

## Observables in muon capture on $^{23}\text{Na}$ and the effective weak couplings $\tilde{g}_a$ and $\tilde{g}_p$

B. L. Johnson,<sup>1</sup> T. P. Gorringer,<sup>1</sup> D. S. Armstrong,<sup>2</sup> J. Bauer,<sup>1</sup> M. D. Hasinoff,<sup>3</sup> M. A. Kovash,<sup>1</sup> D. F. Measday,<sup>3</sup>  
B. A. Moftah,<sup>3</sup> R. Porter,<sup>1</sup> and D. H. Wright<sup>4</sup>

<sup>1</sup>*Department of Physics and Astronomy, University of Kentucky, Lexington, Kentucky 40506*

<sup>2</sup>*Department of Physics, College of William and Mary, Williamsburg, Virginia 23187*

<sup>3</sup>*Department of Physics and Astronomy, University of British Columbia, Vancouver, British Columbia, Canada V6T 1Z1*

<sup>4</sup>*TRIUMF, 4004 Wesbrook Mall, Vancouver, British Columbia, Canada V6T 2A3*

(Received 4 June 1996)

We report measurements of capture rates and hyperfine dependences in muon capture on  $^{23}\text{Na}$  to various states in Ne and F isotopes. We also report comparisons of the capture rates and hyperfine dependences for six  $^{23}\text{Na} \rightarrow ^{23}\text{Ne}$  transitions with the  $1s-0d$  shell model with the empirical effective interaction of Brown and Wildenthal and the realistic effective interaction of Kuo and Brown. Fits to the data with the Brown and Wildenthal interaction yield an effective coupling  $\tilde{g}_a = -1.01 \pm 0.07$  and an effective coupling ratio  $\tilde{g}_p/\tilde{g}_a = 6.5 \pm 2.4$ . The value of  $\tilde{g}_a$  is consistent with values of  $\tilde{g}_a$  extracted from  $\beta^+/\beta^-$  decay and  $(p,n)/(n,p)$  charge exchange data, and the value of  $\tilde{g}_p/\tilde{g}_a$  is consistent with the predictions of PCAC and pion-pole dominance. We evaluate the nuclear model dependence of these values of  $\tilde{g}_a$  and  $\tilde{g}_p/\tilde{g}_a$  and examine the role of the Gamow-Teller and other matrix elements in the  $^{23}\text{Na} \rightarrow ^{23}\text{Ne}$  transitions. [S0556-2813(96)05911-0]

PACS number(s): 23.40.Bw, 11.40.Ha, 23.40.Hc, 27.30.+t

### I. INTRODUCTION

In the absence of second class currents the nucleon's weak axial current has the general form

$$J_{\mu 5}^{\pm} = [F_A(q^2)\gamma_5\gamma_{\mu} - iF_P(q^2)\gamma_5q_{\mu}]\tau^{\pm}, \quad (1)$$

where  $q_{\mu}$  is the four-momentum transfer and  $F_A(q^2)$  and  $F_P(q^2)$  are the axial and induced pseudoscalar form factors. The corresponding axial and induced pseudoscalar coupling constants are defined in terms of their form factors by  $g_a = F_A(0)$  and  $g_p = m_{\mu}F_P(0 + 0.9m_{\mu}^2)$  respectively. The dynamics of the nucleon's weak axial current (how the nucleon's weak interaction is dressed by the nucleon's strong interaction) are encoded in the form factors  $F_A(q^2)$  and  $F_P(q^2)$  and the coupling constants  $g_a$  and  $g_p$ .

Two basic assumptions, partial conservation of the axial current (PCAC) [1,2] and the pion-pole dominance of the induced pseudoscalar form factor, render a simple relationship between the form factors  $F_A(q^2)$  and  $F_P(q^2)$  [3]

$$F_P(q^2) = \frac{2m_{\mu}MF_A(0)}{m_{\pi}^2 + q^2}, \quad (2)$$

and the prediction  $g_p/g_a = 6.7$  ( $m_{\mu}$ ,  $m_{\pi}$ , and  $M$  are the muon, pion, and nucleon masses). PCAC is grounded in the  $SU(2)_L \times SU(2)_R$  chiral symmetry of QCD and the relationship of the pion to its spontaneous and explicit symmetry breaking. Pion-pole dominance of  $F_P(q^2)$  is grounded in the assumption that one-pion exchange dominates heavy meson and multimeson exchange between the hadronic and leptonic currents in semileptonic weak processes. The world average value of  $g_p/g_a$  extracted from measurements of ordinary muon capture on hydrogen is  $g_p/g_a = 6.9 \pm 1.5$  [4], consistent with Eq. (2) and the assumptions of PCAC and pion-pole dominance.

The nonconservation of the nucleon's weak axial current permits the renormalization of  $g_a$  and  $g_p$  in nuclear matter. In the impulse approximation the nuclear weak current is the sum of  $A$  one-body nucleon weak currents, the effects of two- through many-body currents being incorporated by replacing the free nucleon couplings  $g_a$  and  $g_p$  with effective nucleon couplings  $\tilde{g}_a$  and  $\tilde{g}_p$ . A number of authors have explored the renormalization  $\tilde{g}_a$  and  $\tilde{g}_p$  due to various effects from meson exchange currents and  $\Delta$  excitations [5-7] to the partial restoration of chiral symmetry [8]. Long ago Ericson and co-workers [5,6] investigated  $p$ -wave pion exchange currents and predicted quenching factors of 0.70 and 0.33 for  $\tilde{g}_a$  and  $\tilde{g}_p$  in infinite nuclear matter. In finite nuclear matter they anticipated an increasing quenching with increasing mass towards the limiting values of infinite nuclear matter. Recently Delorme and Ericson [7] augmented the  $p$ -wave pion exchange currents with  $s$ -wave pion exchange currents and obtained quenching factors of 0.70 and 0.60 for  $\tilde{g}_a$  and  $\tilde{g}_p$  in infinite nuclear matter. In either case the effective weak couplings  $\tilde{g}_a$  and  $\tilde{g}_p$  are interesting and complementary probes of non-nucleonic effects in nuclei.

The established probe of  $\tilde{g}_p$  is nuclear muon capture. The role of the induced pseudoscalar coupling in weak processes is governed by  $q/M$  and is therefore negligible in  $\beta$  decay (where  $q/M \sim 0.001$ ) but significant in  $\mu$  capture (where  $q/M \sim 0.1$ ). Existing studies of  $\tilde{g}_p$  include measurements of observables in inclusive and exclusive  $\mu^-$  capture as well as ordinary and radiative  $\mu^-$  capture. The challenge is to measure observables in  $\mu^-$  capture with as large a  $\tilde{g}_p$  dependence and as small a nuclear-model dependence as possible. The current status of the experimental determinations of  $\tilde{g}_p$  is rather intriguing.

The most celebrated determination of  $\tilde{g}_p$  concerns the  $^{12}\text{C}(0^+, 0)(\mu^-, \nu)^{12}\text{B}(1^+, 0)$  transition. Utilizing novel techniques, groups at PSI [9,10] and KEK [11,12] have measured

both the longitudinal and average polarizations ( $P_1$  and  $P_{\text{av}}$ ) of the  $^{12}\text{B}$  recoil. Compared to muon capture rates,  $P_1$  and  $P_{\text{av}}$  offer a greater sensitivity to  $\tilde{g}_p$  and a lesser sensitivity to nuclear model uncertainties since they are governed by the relative, not absolute, capture rates to the  $^{12}\text{B}$  magnetic substates. The most recent extraction of  $\tilde{g}_p$  from the  $P_1$  and  $P_{\text{av}}$  data using the  $0p$  shell model, Cohen-Kurath effective interaction, and Woods-Saxon wave functions yields  $\tilde{g}_p/\tilde{g}_a = 8.5 \pm 1.9$  or  $9.7 \pm 1.7$ , consistent with Eq. (2) and the assumptions of PCAC and pion-pole dominance (the different values correspond to different measurements of muon capture rates to  $^{12}\text{B}$  excited states). This conclusion is strengthened by the agreement of the measured and calculated  $^{12}\text{C}(0^+, 0) \leftrightarrow ^{12}\text{B}(1^+, 0) \mu^-$  capture rate and  $\beta^+$ -decay rate.

While ordinary muon capture (OMC) is a spacelike process with  $q^2 \sim +m_\mu^2$  in the domain of high-energy photons, radiative muon capture (RMC) is mainly a timelike process with  $q^2 \sim -m_\mu^2$ . Consequently, RMC is closer than OMC to the pion pole and  $\tilde{g}_p$  plays a much larger role in the radiative process than the ordinary process. This led to proposals to extract  $\tilde{g}_p$  from the ratio of inclusive RMC to inclusive OMC. The ratio  $R$  promised a high sensitivity to  $\tilde{g}_p$  and a lower sensitivity to nuclear model uncertainties than either the inclusive RMC or OMC rates. Recently, experimental work at PSI [14,15] and TRIUMF [16,17] have accumulated a large body of data for inclusive radiative muon capture rates on nuclei from  $^{12}\text{C}$  to  $^{209}\text{Bi}$  that indicate  $R$  decreases systematically as  $A$  increases. A variety of nuclear models (phenomenological [18,19], Fermi-gas [20,21], shell model [22–24], and RPA sum rules [25]) have been used to extract  $\tilde{g}_p$  from the RMC/OMC data and, at face value, suggest a progressive and substantial quenching of  $\tilde{g}_p$  from light to heavy nuclei (as predicted by Ref. [6]). However, the nuclear model uncertainties in the extraction of  $\tilde{g}_p$  from  $R$ , epitomized by  $\tilde{g}_p/\tilde{g}_a$  values of  $7.3 \pm 0.9$  [19] and  $13.6^{+1.6}_{-1.9}$  [22] obtained with two different models using the same  $^{16}\text{O}$  data, make claims of a progressive and substantial quenching of  $\tilde{g}_p$  controversial. Whether  $\tilde{g}_p$  is or is not renormalized in nuclei is the subject of lively debate.

In this paper we report measurements of capture rates and hyperfine dependences in muon capture on  $^{23}\text{Na}$  to various states in Ne and F isotopes. The main goal was an extraction of the effective couplings  $\tilde{g}_a$  and  $\tilde{g}_p/\tilde{g}_a$  from the capture rates and hyperfine dependences of the six observed  $^{23}\text{Na}(\mu^-, \nu) ^{23}\text{Ne}^*$  transitions, including an evaluation of the nuclear model dependence of the effective coupling constants. The paper is organized as follows. Section II is an overview of the hyperfine effect in nuclear muon capture, Sec. III describes the experimental setup, Secs. IV and V describe the analysis and results of the experiment, and Sec. VI deals with the extraction of  $\tilde{g}_a$  and  $\tilde{g}_p/\tilde{g}_a$  from the capture rate and hyperfine dependence data and their nuclear model dependence. We have previously published values of  $\tilde{g}_p/\tilde{g}_a$  extracted from the hyperfine dependences of two of these transitions,  $^{23}\text{Na}(3/2^+, 0)(\mu^-, \nu) ^{23}\text{Ne}(1/2^+, 1017)$  and  $^{23}\text{Na}(3/2^+, 0)(\mu^-, \nu) ^{23}\text{Ne}(3/2^+, 1823)$ , in Ref. [26].

## II. HYPERFINE EFFECT IN NUCLEAR MUON CAPTURE

For nonzero spin ( $J_i \neq 0$ ) nuclei the  $1S$  state of the muonic atom is split into two hyperfine (HF) states

$F_+ = J_i + 1/2$  and  $F_- = J_i - 1/2$ ; in nuclei with positive magnetic moments the  $F_-$  state is the true ground state and in nuclei with negative magnetic moments the  $F_+$  state is the true ground state. The capture rates from the  $F_-$  and  $F_+$  states, denoted  $\Lambda^-$  and  $\Lambda^+$ , are in general different and it has long been recognized that the hyperfine dependence  $\Lambda^+/\Lambda^-$  can be rather sensitive to  $\tilde{g}_p/\tilde{g}_a$  and rather insensitive to nuclear model uncertainties (see for example the review of Mukhopadhyay [27]).

The physics of the  $\tilde{g}_p/\tilde{g}_a$  sensitivity and nuclear model insensitivity of  $\Lambda_+/\Lambda_-$  is nicely demonstrated in the Fujii-Primakoff approximation [28] where only the Fermi (F) and Gamow-Teller (GT) nuclear matrix elements are employed. For the example of a  $3/2^+ \rightarrow 1/2^+$  ( $J_i \rightarrow J_f$ ) transition the Fujii-Primakoff approximation for  $\Lambda^-/\Lambda^+$  yields (see for example Ref. [27])

$$\Lambda^+/\Lambda^- = \frac{G_p^2}{8(\frac{1}{3}G_p - G_a)^2 + \frac{1}{9}G_p^2}, \quad (3)$$

where  $G_A$  and  $G_P$  are the so-called Fujii-Primakoff effective coupling constants

$$G_a = -[g_a + (q/2M)(g_v + g_m)], \quad (4)$$

$$G_p = -(q/2M)(g_p - g_a + g_v + g_m),$$

and  $g_v$  and  $g_m$  are the vector and weak magnetic coupling constants of the weak vector current. Equation (3) is strongly dependent on  $\tilde{g}_p/\tilde{g}_a$  and, due to the cancellation of the GT matrix element in the  $\Lambda^-/\Lambda^+$  ratio, is independent of the nuclear model.

Of course, although the Fujii-Primakoff approximation is a useful guide, a full calculation employing matrix elements beyond the Fermi and Gamow-Teller matrix elements is necessary to extract  $\tilde{g}_p/\tilde{g}_a$  from  $\Lambda^+/\Lambda^-$ . In the literature there are a number of calculations of  $\Lambda^+/\Lambda^-$  for exclusive OMC including the groundbreaking work of Walecka for  $^7\text{Li}$  [29] and Bernébeu for  $^{11}\text{B}$  [30] and the more recent studies of Koshigiri, Ohtsubo, and Morita [31,32] for  $^{11}\text{B}$  and  $^{13}\text{C}$  and Kuz'min *et al.* [33] for  $^9\text{Be}$ ,  $^{10}\text{B}$ , and  $^{11}\text{B}$ . Generally the full calculations show that  $\Lambda^-/\Lambda^+$  retains a relatively strong dependence on  $\tilde{g}_p/\tilde{g}_a$  and a relatively weak dependence on the nuclear model. However, when the GT matrix element is small the arguments for strong  $\tilde{g}_p/\tilde{g}_a$  sensitivity and weak nuclear model sensitivity collapse.

The  $1S$  state of the  $\mu$  atom is formed with the  $F_+$  and  $F_-$  hyperfine states statistically populated [34], i.e.,  $f_+ = (J_i + 1)/(2J_i + 1)$  and  $f_- = J_i/(2J_i + 1)$ . However, during the  $\mu$  atom's lifetime,  $M1$  Auger transitions cause the upper HF state to deexcite to the lower HF state. The rate of hyperfine transitions  $\Lambda_h$  is governed by the overlap of the muon and nuclear wave functions and the relative size of the hyperfine splitting and electronic binding energies. The former leads to a systematic increase in  $\Lambda_h$  with  $Z$  while the latter leads to sudden decreases in  $\Lambda_h$  when the increasing hyperfine splitting with increasing atomic number halts  $K$  shell emission at  $Z \sim 6$ ,  $L$  shell emission at  $Z \sim 18$ , etc. Measurements of  $\Lambda_h$  have been performed for muonic atoms of  $0p$ -shell [35–37] and  $1s-0d$  shell nuclei [39,38,40,41], and

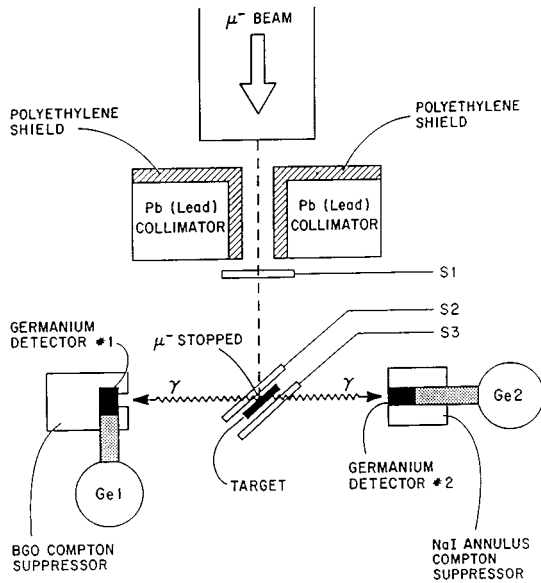


FIG. 1. Schematic view of the experimental setup showing the  $\mu^-$  beam and collimation, the beam scintillators (S1, S2, and S3), the  $^{23}\text{Na}$  target, the Ge detectors (Ge1 and Ge2) and their Compton suppressors (CS1 and CS2).

for several atoms, for example muonic  $^{11}\text{B}$  and  $^{19}\text{F}$ , the hyperfine transition rate  $\Lambda_h$  is of the order of the muon disappearance rate  $\Lambda_D$ .

A method of measuring the hyperfine dependence of  $\mu^-$  capture, exploiting the hyperfine transitions from the upper to lower HF states and consequently a  $\mu^-$  capture time dependence that is a function of  $\Lambda^+/\Lambda^-$ , was pioneered for inclusive OMC by Winston and Telegdi [38,39] and exclusive OMC by Deutsch *et al.* [35]. In the work of Winston *et al.* the hyperfine dependence of inclusive  $\mu^-$  capture on  $^{19}\text{F}$  was obtained from the neutron time spectra and the result,  $\Lambda^+/\Lambda^- = 0.3 \pm 0.1$ , established the V-A character of  $\mu^-$  capture. In the work of Deutsch *et al.* the hyperfine dependence of the  $^{11}\text{B}(3/2^-, 0) \rightarrow ^{11}\text{Be}(1/2^-, 320)$  transition was obtained from the 320 keV  $\gamma$ -ray time spectra and the result,  $\Lambda^+/\Lambda^- < 0.17$ , yielded an upper limit on the pseudoscalar coupling  $\tilde{g}_p < 12$ .

A major part of this work is a study of the hyperfine dependence of exclusive  $\mu^-$  capture on  $^{23}\text{Na}$ . Like the cases of muonic  $^{11}\text{B}$  and  $^{19}\text{F}$ , the hyperfine transition rate in  $^{23}\text{Na}$  is conducive to hyperfine dependence measurements [26,41]. Further, muon capture on  $^{23}\text{Na}$  offers a number of Gamow-Teller transitions that, in conjunction with the highly successful  $1s-0d$  shell model and USD empirical interaction, make a promising case for the extraction of  $\tilde{g}_a/\tilde{g}_p$  from the measurement of  $\Lambda^+/\Lambda^-$ .

### III. EXPERIMENTAL SETUP

#### A. Beam, target, and detector setup

The experiment was performed on the *M9B* decay-muon beamline at the TRIUMF cyclotron. Figure 1 is a schematic view of the experimental arrangement.

After collimation, the  $\mu^-$  beam yielded a stop rate of  $1.1 \times 10^5/\text{sec}$  in a  $5 \text{ cm} \times 5 \text{ cm}$  beam spot and a 5% ( $\sigma$ )

momentum bite with electron and pion contamination of  $\sim 20\%$  and  $< 0.2\%$ , respectively. The collimator was constructed of Pb bricks lined with  $\text{CH}_2$  sheet; the lining preventing the production of high-energy muonic x rays by stopping muons in  $\text{CH}_2$  not Pb. The  $^{23}\text{Na}$  target was a 5.0 cm diameter and 0.5 cm thick disk of pure metallic sodium packed in a thin-walled polyethylene container under a  $\text{N}_2$  atmosphere. The target was angled at  $45^\circ$  to the beam and detector axes in order to maximize muon stops and minimize  $\gamma$  absorption.

Three plastic scintillators, S1 mounted on the downstream face of the collimator, S2 and S3 mounted on the upstream and downstream faces of the target respectively, defined a muon stop via the logic  $S1 \cdot S2 \cdot S3$ . Their energy thresholds were set above minimally-ionizing particles in order to distinguish muons from electrons.

Two high-purity *n*-type Ge detectors, Ge1 and Ge2, viewed the target at  $90^\circ$  to the beam axis. Ge1 was a 33% efficiency detector with in-beam time and energy resolutions (FWHM) of 7.5 ns and 2.7 keV at 1.33 MeV. Ge2 was a 40% detector with in-beam time and energy resolutions (FWHM) of 12.5 ns and 2.8 keV at 1.33 MeV. Ge1 and Ge2 were located at distances of approximately 12 cm and 14 cm, respectively, from the target center, a compromise between the detector acceptances and resolutions. Typical singles rates above their 400 keV energy thresholds were  $1 \times 10^3/\text{sec}$  in Ge1 and  $2 \times 10^3/\text{sec}$  in Ge2.

Surrounding the two Ge detectors, Ge1 and Ge2, were two Compton suppressors, CS1 and CS2. CS1 was a ten-element array of optically isolated BGO crystals and CS2 was a six-element annulus of optically isolated NaI crystals. The in-beam time resolutions ( $\sigma$ ) were approximately 15 ns for CS1 (BGO) and 20 ns for CS2 (NaI) and the in-beam energy resolutions ( $\sigma$ ) were 40% for CS1 and 15% for CS2. The purpose of CS1 and CS2 was two-fold. Firstly, used as a veto on their own Ge detector (i.e.,  $\text{Ge1} \cdot \text{CS1}$  and  $\text{Ge2} \cdot \text{CS2}$ ) they reduced the continuum background due to Compton scattering. Secondly, used in coincidence with the opposing Ge detector (i.e.,  $\text{Ge1} \cdot \text{CS2}$  and  $\text{Ge2} \cdot \text{CS1}$ ) they identified  $\gamma$ - $\gamma$  cascades. Under beam conditions CS1 and CS2 afforded signal-to-noise improvements of a factor of 3 for Ge1 and a factor of 4 for Ge2.

#### B. Electronics

An event was defined as the OR of the logic signals  $\text{Ge1} \cdot \text{CS1} \cdot \mu\text{STOP} \cdot \text{busy}$ , and  $\text{Ge2} \cdot \text{CS2} \cdot \mu\text{STOP} \cdot \text{busy}$ , where Ge1 and Ge2 indicate signals in the Ge detectors, CS1 and CS2 indicate the absence of signals in the corresponding Compton suppressors,  $\mu\text{STOP}$  indicates one or more stopped muons in the previous 2.0  $\mu\text{sec}$ , and busy indicates the data acquisition system was live. The veto signals CS1 and CS2 were the outputs of ten-fold or six-fold OR's of discriminators on each of the ten or six elements of the suppressors CS1 and CS2. The discriminator thresholds were set to  $\sim 500$  keV and the veto widths were set to 80 ns. The  $\mu\text{STOP}$  signal was the output of a 2.0  $\mu\text{s}$  updating gate that was set by  $S1 \cdot S2 \cdot S3$ . The receipt of an event initiated the digitizing and recording of the energy and time signals

from Ge detectors, Compton suppressors and beam scintillators, a 5  $\mu\text{sec}$  history of muon stops in the target, and various diagnostic information.

The energy signals from Ge1 and Ge2 were processed by a pair of Tennelec TC-243A spectroscopy amplifiers and digitized by a pair of LeCroy 3512 buffered ADC's. To minimize distortions the energy signals were processed and digitized in the experimental area rather than the counting room. To optimize the spectroscopy amplifier shaping constants and pole zeros they were adjusted under beam-on conditions.

The timing signals from the Ge detectors were generated by a coincidence between a pair of constant fraction discriminators (CFD's) on each Ge timing circuit. One of each CFD pair, Ge1<sup>lo</sup> and Ge2<sup>lo</sup> with the lower thresholds, determined the timing for the coincidence output, and the other of each CFD pair, Ge1<sup>hi</sup> and Ge2<sup>hi</sup> with the higher threshold, determined the  $\sim 400$  keV energy threshold for the coincidence output. Their coincidences Ge1<sup>lo</sup>·Ge1<sup>hi</sup> and Ge2<sup>lo</sup>·Ge2<sup>hi</sup> then defined the logic signals Ge1 and Ge2, respectively. In addition, a series of leading-edge discriminators (with thresholds of approximately 100, 250, 500, and 750 keV) generated a series of timing signals (known as LE1 through LE4) to provide pulse-shape information for Ge1 and Ge2.

The 5  $\mu\text{sec}$  history of muon stops in the target was obtained using a router box. The router box consisted of one input, a 5  $\mu\text{sec}$  cable-delayed S1·S2·S3, one gate, a 5  $\mu\text{sec}$  wide pulse generated by an event, and four outputs,  $T_{\mu 1}$  through  $T_{\mu 4}$ . The output  $T_{\mu 1}$  corresponded to the first delayed S1·S2·S3 in the gate, the output  $T_{\mu 2}$  corresponded to the second delayed S1·S2·S3 in the gate, and so on. The four outputs fed four TDC channels that digitized the time of the first, second, third, and fourth delayed S1·S2·S3 pulses. If more than four S1·S2·S3 pulses occurred within the gate only the first four S1·S2·S3 pulses were recorded. The arrangement acted as a four-hit capacity multihit TDC.

Lastly, also digitized and recorded on receipt of an event were the individual amplitude and ORed timing signals from the two suppressor arrays, amplitude and timing signals from the S1, S2, and S3 beam scintillators, and bits indicating previous Ge pulses within 50  $\mu\text{sec}$  (known as the pile-up bits PUP1 and PUP2) and previous huge Ge pulses ( $E > 10$  MeV) within 500  $\mu\text{sec}$  (known as the overload bits OVLD1 and OVLD2).

#### IV. DATA REDUCTION

During the experiment data were collected from a total of  $\sim 1 \times 10^{11}$   $\mu^-$  stops in  $^{23}\text{Na}$ ,  $\sim 2 \times 10^{10}$   $\mu^-$  stops in  $^{31}\text{P}$  (for background studies), and about  $\sim 1 \times 10^9$   $\mu^-$  stops each in Ca, Fe, and Pb (for Ge detector acceptance and resolution studies). Beam-on and beam-off  $^{22}\text{Na}$ ,  $^{60}\text{Co}$ , and  $^{137}\text{Cs}$  source calibration data were also collected. In this section we describe the offline cuts and corrections applied to the raw data and the determination of the Ge1 and Ge2 energy and time resolution functions and acceptances.

##### A. Cuts and corrections

An important source of background in the Ge detectors is Compton scattering. In the analysis the hardware rejection of

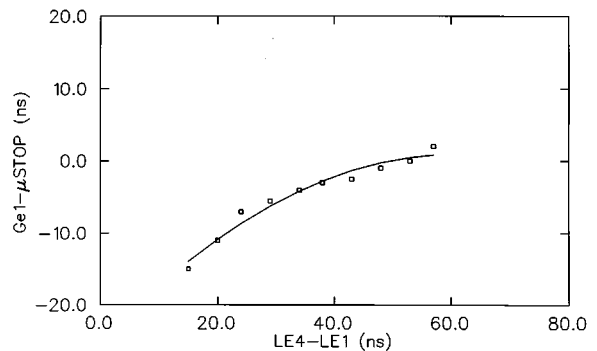


FIG. 2. Plot of Ge1- $\mu\text{STOP}$  (the time between the incoming muon and outgoing photon) vs LE4-LE1 (a measure of the Ge pulse risetime) for the  $L_{\alpha}$  x rays of muonic lead. The correlation between LE4-LE1 and Ge- $\mu\text{STOP}$  is a result of time walk (a horizontal line would indicate the absence of time walk).

Ge signals with corresponding suppressor signals above  $\sim 500$  keV was extended with the software rejection of Ge signals with corresponding suppressor signals above  $\sim 100$  keV. The signal-to-noise improvement, due to the software Compton suppression, was approximately a factor of 5 for Ge1 and 3 for Ge2.

A source of degradation of the energy resolution of the Ge detectors is pulse pileup. Events were rejected in the analysis if either the Ge detector's corresponding pileup bit (PUP1 or PUP2) or overload bit (OVLD1 or OVLD2) were set. The resulting improvement in the energy resolution was negligible in the full width half maximum but significant ( $\sim 20\%$ ) in the full width tenth maximum. A second source of degradation of the energy resolution of the Ge detectors was long-timescale drifts in the gains and pedestals during the experiment. To correct these long-timescale drifts we employed a gain and pedestal stabilization procedure. The stabilization procedure consisted of the monitoring of the centroids of several strong  $\gamma$ -ray peaks to measure and correct gain and pedestal shifts during the experiment. We used the 511 keV  $e^+e^-$  annihilation peak and the 1274 and 2127 keV ( $\mu^-, n\nu$ ) capture peaks and determined their centroids every 200 000 events or roughly every 500 sec. This stabilization procedure yielded a FWHM improvement of 0.2 keV in Ge1 and 0.3 keV in Ge2.

Despite the use of constant fraction discriminators in the Ge1 and Ge2 timing circuitry pulse-shape variations led to some residual time walk. This is illustrated in Fig. 2 where Ge- $\mu\text{STOP}$ , the time difference between the incoming muon and outgoing photon, is plotted versus LE4-LE1, a measure of the Ge signal risetime, for the Fe  $L_{\alpha}$  muonic x ray. In Fig. 2 small values of LE4-LE1 correspond to fast risetime Ge pulses and large values of LE4-LE1 correspond to slow risetime Ge pulses and the presence of time walk is indicated by the presence of correlations between LE4-LE1 and Ge1- $\mu\text{STOP}$  times (the absence of time walk would be indicated by a horizontal line).

Using the spectra of Ge- $\mu\text{STOP}$  versus LE4-LE1 we were able to parametrize the Ge signal time walk for the prompt x ray data and then correct the Ge signal time walk for delayed  $\gamma$ -ray data. To do this plots similar to Fig. 2 were generated for a number of muonic x rays (579 keV Cl  $K_{\alpha}$ ,

938 keV Pb  $M_\alpha$ , 1255 keV Fe  $K_\alpha$ , and 2500 keV Pb  $L_\alpha$ ) and for both Ge detectors. The resulting curves were fit to the quadratic  $\alpha + \beta t + \gamma t^2$  where the coefficients  $\alpha$ ,  $\beta$ , and  $\gamma$  characterized the Ge signal time walk and its energy dependence (actually, no significant energy dependence in  $\alpha$ ,  $\beta$ , and  $\gamma$  for either Ge1 or Ge2 was observed). Using the ‘‘best fit’’ values of  $\alpha$ ,  $\beta$ , and  $\gamma$  determined from the x-ray data, the time walk corrections were made to the  $\gamma$ -ray data.

The cuts and corrections described above were used to sort the data and generate the necessary energy and time spectra for the subsequent analysis.

### B. Ge energy and time instrumental line shapes

To determine the Ge1 and Ge2 energy resolution functions,  $R_1(E)$  and  $R_2(E)$ , we used a number of high statistics, background-free, Doppler-free  $\gamma$  rays between the energies of 500 and 3000 keV. For both Ge1 and Ge2 the resolution functions were taken as the sum of a main Gaussian peak and a satellite Gaussian peak — the sum conveniently representing the low-energy tails in  $R_1(E)$  and  $R_2(E)$ . The parameters of the resolution functions, the relative amplitude and relative position of the two peaks  $r_E$  and  $x_E$ , and the widths of the main and satellite peaks  $\sigma_E^m$  and  $\sigma_E^s$ , were obtained from fits of  $R_1(E)$  and  $R_2(E)$  to the  $\gamma$ -ray line shapes. The energy dependence of the resolution functions were therefore determined by the energy dependence of the parameters  $r_E$ ,  $x_E$ ,  $\sigma_E^m$ , and  $\sigma_E^s$ . It was found for both Ge1 and Ge2 that  $\sigma_E^m$  increased smoothly with energy while the remaining parameters were essentially energy independent. At 1.33 MeV the Ge1 and Ge2 FWHM were 2.7 keV and 2.8 keV and FWTM were 4.8 keV and 6.7 keV.

To determine the Ge1 and Ge2 time resolution functions,  $R_1(t)$  and  $R_2(t)$ , we measured muonic x-ray time spectra from a variety of targets (P, Ca, Fe, and Pb) between the energies of 500 and 3000 keV. The muonic x rays are produced promptly and are ideal for determining  $R_1(t)$  and  $R_2(t)$ . As for the  $\gamma$ -ray energy spectra the x-ray time spectra were fitted to the sum of a main Gaussian peak and a satellite Gaussian peak — the sum conveniently representing the early-time tails in the time resolution functions. The parameters in the fits were the position of the main peak  $t_o$ , the relative amplitude and relative position of the satellite peak  $r_t$  and  $x_t$ , and the widths of the main and satellite peaks  $\sigma_t^m$  and  $\sigma_t^s$ . The energy dependence of the parameters  $t_o$ ,  $r_t$ ,  $x_t$ ,  $\sigma_t^m$ , and  $\sigma_t^s$  therefore determined the energy dependence of  $R_1(t)$  and  $R_2(t)$ . In the case of Ge1 it was found that  $t_o$  shifted by  $\sim 1.4$  ns and  $\sigma_t^s$  narrowed by  $\sim 0.9$  ns from 1000 to 3000 keV while  $r_t$ ,  $x_t$ , and  $\sigma_t^m$  were essentially energy independent. In the case of Ge2 it was found that  $\sigma_t^s$  narrowed by  $\sim 1.8$  ns from 1000 to 3000 keV while  $t_o$ ,  $r_t$ ,  $x_t$ , and  $\sigma_t^m$  were essentially energy independent. For both Ge1 and Ge2 the energy dependences of the energy dependent parameters were found to be reasonably represented by functions of the form  $t_o = a + be^{-cE}$ . Above 1000 keV the FWHM of the time resolutions of Ge1 and Ge2 were better than 10 ns and 13 ns, respectively.

### C. $\gamma$ -ray Doppler line shapes

The recoil nucleus following  $\mu^-$  capture on  $^{23}\text{Na}$  has a velocity of  $\sim 0.005$  c. Consequently, when the recoil’s

$\gamma$ -ray lifetime  $\tau_d$  is short or comparable to the recoil’s stopping time  $\tau_s$ , the observed  $\gamma$ -rays are Doppler broadened. For the Ne and F isotopes produced in  $\mu^-^{23}\text{Na}$  the value of  $\tau_s$  in the sodium target was about  $10^{-12}$  s.

In the case of the two-body final state in the  $(\mu^-, \nu)$  reaction the recoil’s initial velocity is fixed. Formulas for the Doppler line shapes appropriate to the  $(\mu^-, \nu)$  reaction and circumstances where  $\tau_s \gg \tau_d$  and  $\tau_s \sim \tau_d$  have been given by Grenacs *et al.* [42] and Pratt [43]. In the case of the three-body final state in the  $(\mu^-, n\nu)$  reaction the recoil’s initial velocity is a continuous distribution. Expressions for the Doppler line shapes appropriate to the  $(\mu^-, n\nu)$  reaction have been given by Miller [44] for the cases of (1) a two-step process involving the reaction  $[Z, A](\mu^-, \nu)[Z-1, A]$  followed by neutron emission, and (2) a direct neutron emission process  $[Z, A](\mu^-, n\nu)[Z-1, A-1]$ .

In fits to Doppler broadened  $\gamma$  rays we used resolution functions  $R_1(E)$  and  $R_2(E)$  convoluted with the appropriate Doppler line shapes of Refs. [42–44]. We varied the parameters of the Doppler line shapes, for example the  $\gamma$ -recoil angular correlation coefficients, to obtain the best fit.

### D. Ge detector acceptances

To determine the acceptances of Ge1 and Ge2 as a function of energy,  $\epsilon\Delta\Omega_1(E)$  and  $\epsilon\Delta\Omega_2(E)$ , we used the intensities of the muonic x rays from the P, Ca, Fe, and Pb targets. In the case of the muonic P and Fe x ray data we employed the  $K_\alpha$ ,  $K_\beta$ ,  $K_\gamma$ , and  $K_\delta$  transitions and the yield determinations of Hartmann *et al.* [45] for  $\mu^-$ -Fe and Vogel [46] for  $\mu^-$ -P. In the case of the muonic Pb x-ray data we employed the  $L_\alpha$  and  $M_\alpha$  transitions and extrapolated the yield determinations of Hartmann *et al.* [47] for muonic atoms between  $Z=49$  and 79 to  $Z=82$ . The yields from the  $Z=49$  to 79 muonic atoms varied by  $\pm 3\%$  for the  $L_\alpha$  and  $\pm 7\%$  for the  $M_\alpha$  so the extrapolation is probably better for the  $L_\alpha$  than the  $M_\alpha$ . In the case of the muonic Ca x-ray data we employed the sum of the yields of the  $K$  series x-ray transitions.

Using the P, Ca, Fe, and Pb x-ray data the Ge detector acceptances were computed via

$$\epsilon\Delta\Omega = \frac{N_x}{N_\mu Y_x f_{ab} f_{sv}}, \quad (5)$$

where  $N_x$  is the number of counts in the x-ray peak,  $N_\mu$  is the number of livetime-corrected muon stops,  $Y_x$  is the appropriate x-ray or x-ray series yield per muon stop, and  $f_{ab}$  and  $f_{sv}$  are correction factors that account for the absorption of x rays in the target and the self-vetoing of x rays by the Compton suppressors, respectively. The factor  $f_{ab}$  was calculated using the  $\gamma$ -ray absorption tables of Storm and Israel [48] and its values differed from unity by less than a few percent (the exception was the  $M_\alpha$  in  $\mu^-$ -Pb where, due to the large Pb absorption and the low x-ray energy,  $f_{ab}$  was 0.80). The self-veto correction factor  $f_{sv}$  is discussed in detail in Sec. IV E and its values differed from unity by amounts from 3% to 15%.

The resulting determinations of the Ge1 acceptance are plotted as a function of energy in Fig. 3 along with a fit to the curve  $A_1/(B_1 + E_\gamma)$ . The curve, and the ‘‘best fit’’ values of the coefficients  $A_1$  and  $B_1$  for Ge1 and  $A_2$  and  $B_2$  for Ge2,

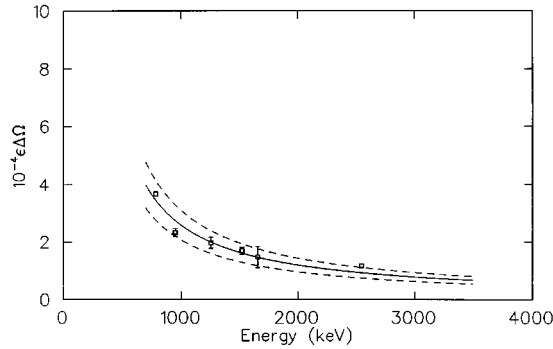


FIG. 3. The Ge1 acceptance versus  $\gamma$ -ray energy obtained from the muonic P, Ca, Fe, and Pb x-ray data. The solid line is the “best fit” of the curve  $A_1/(B_1+E_\gamma)$  to the x-ray data and the dashed lines are a conservative estimate of the uncertainty in the acceptance.

were used to parameterize the Ge1 and Ge2 acceptances in the subsequent data analysis. Based on the uncertainties in the x-ray counts and yields, the number of muon stops, and the correction factors  $f_{ab}$  and  $f_{sv}$ , we obtained a conservative uncertainty of  $\sim 20\%$  in the Ge1 and Ge2 acceptances.

#### E. Self-veto correction factor $f_{sv}$

A significant correction in determining the yields of both x rays and  $\gamma$  rays was self-vetoing. Self-vetoing occurs when a valid x-ray or  $\gamma$ -ray signal in Ge1 or Ge2 is rejected due to a signal in the surrounding Compton suppressor CS1 or CS2. This self-vetoing may result from prompt coincidences (for example when a  $\gamma$ -ray cascade results in the detection of one  $\gamma$  ray in the Ge detector and another  $\gamma$  ray in the Compton suppressor), delayed coincidences (for example when a delayed  $\gamma$  ray is detected in the Ge detector and a prompt x ray is detected in the Compton suppressor), or random coincidences (when unrelated  $\gamma$  rays are detected in the Ge detector and Compton suppressor). The amount of self-vetoing is, therefore, dependent on the detector, target and transition, and must be determined for each x ray and  $\gamma$  ray.

To determine the Ge1 self-veto correction factor we measured, for each x-ray and  $\gamma$ -ray, the ratio of the counts in the Ge1 singles and Ge1·CS2 coincidence spectra. This ratio determines the fraction of Ge1 events that have a CS2 coincidence that is proportional to the fraction of Ge1 events that had a CS1 coincidence ( $1-f_{sv}$ ). The proportionality constant between the Ge1·CS2/Ge1 and Ge1·CS1/Ge1 ratios was then obtained from measurements of the coincident  $^{60}\text{Co}$  1.17 and 1.33 MeV  $\gamma$  rays with the Compton suppression logic switched off. Due to the very similar solid angles CS1 and CS2 subtended to the target the proportionality constant was 1.0 and therefore the Ge1 self-veto correction factor  $f_{sv}$  for each  $\gamma$  ray or x ray was computed from  $1-\text{Ge1}\cdot\text{CS2}/\text{Ge1}$ . Similarly, the Ge2 self-veto correction factor  $f_{sv}$  was computed from  $1-\text{Ge2}\cdot\text{CS1}/\text{Ge2}$ .

Lastly, our method for determining the self-veto correction makes the assumption of no angular correlations in the Ge·CS coincidences. However, since the self-veto correction is quite small, errors due to this assumption should be negligible.

## V. RESULTS

A few remarks on notation: in the following sections we discuss  $\gamma$ -ray and state yields, yields due to capture from the  $F_+$ ,  $F_-$  and experimental mixture of HF states, and yields due to direct  $\mu^-$  capture to a state and yields due to direct and indirect  $\mu^-$  capture to a state. By the experimental mixture of HF states we mean the fractional population of the  $F_-$  and  $F_+$  HF states in the 2.0  $\mu\text{s}$   $\mu\text{STOP}$  gate which, due to the hyperfine effect, were 0.97 and 0.03 respectively (see Sec. V D). By direct capture we mean the production of state  $S$  by  $\mu^-$  capture to state  $S$  and by indirect capture we mean the production of state  $S$  by  $\mu^-$  capture to a higher energy state  $S'$ . We will denote  $\gamma$ -ray yields and state yields by  $Y_\gamma$  and  $Y_S$ , yields from the  $F_+$ ,  $F_-$ , and experimental mixture of HF states by  $Y^+$ ,  $Y^-$ , and  $Y^{\text{obs}}$ , respectively, and yields due to direct  $\mu^-$  capture production of a state by an unprimed  $Y$  and yields due to direct and indirect  $\mu^-$  capture production of a state by a primed  $Y'$ . For example,  $Y_\gamma^{\text{obs}}$  refers to the  $\gamma$ -ray yield due to direct and indirect  $\mu^-$  capture from the experimental mixture of  $F_+$  and  $F_-$  states. The same notation is used for  $\mu^-$  capture rates  $\Lambda$ . To obtain the capture rate  $\Lambda$  from the yield  $Y$  we use  $\Lambda = \Lambda_D Y$  where  $\Lambda_D$  is the muon disappearance rate, the sum of the  $\mu^-$  capture and  $\mu^-$  decay rates.

#### A. $\gamma$ -ray yields from $\mu^-$ capture on $^{23}\text{Ne}$

22 muon capture  $\gamma$  rays, from the mass 20, 21, 22, and 23 neon isotopes and mass 20 fluorine isotope, were identified in the  $\mu^-^{23}\text{Na}$  data. They are listed in Table I along with the spins, parities, and energies of their initial and final states. They include nine  $\gamma$  rays due to transitions in  $^{23}\text{Ne}$ , seven  $\gamma$  rays due to transitions in  $^{22}\text{Ne}$ , and three, two, and one  $\gamma$  rays due to transitions in  $^{21}\text{Ne}$ ,  $^{20}\text{F}$ , and  $^{20}\text{Ne}$ , respectively. The  $\gamma$ -ray lines observed in the mass 23 neon isotope are shown in the Fig. 4 energy level diagram. Representative  $\gamma$ -ray energy spectra, illustrating the quality of the data, are shown in Fig. 5.

The yields of the muon capture  $\gamma$  rays were determined using the equation

$$Y_\gamma^{\text{obs}} = \frac{N_\gamma}{N_\mu \epsilon \Delta \Omega f_{ab} f_{sv} f_{lt}}, \quad (6)$$

where  $Y_\gamma^{\text{obs}}$  is the  $\gamma$ -ray yield,  $N_\gamma$  is the counts in the  $\gamma$ -ray peak,  $N_\mu$  is the number of lifetime-corrected muon stops,  $\epsilon \Delta \Omega$  is the Ge detector acceptance at the appropriate  $\gamma$ -ray energy, and  $f_{ab}$ ,  $f_{sv}$ , and  $f_{lt}$  are target absorption, self-veto and muon lifetime correction factors, respectively. For the  $^{23}\text{Na}$   $\gamma$  rays  $f_{ab}$  differed from unity by less than 3% and  $f_{sv}$  differed from unity by amounts from 5% to 15%. The additional factor  $f_{lt}$  in Eq. (6) compared to Eq. (5) corrects for the muon capture  $\gamma$  rays that fall outside the 2.0  $\mu\text{s}$   $\mu\text{STOP}$  gate. Due to the complications of the updating  $\mu\text{STOP}$  logic  $f_{lt}$  was determined by a Monte Carlo simulation and found to be 0.80.

The  $\gamma$ -ray counts  $N_\gamma$  were obtained from fits to the  $\gamma$ -ray peaks using the energy resolution functions described in Sec. IV B and the resulting  $\gamma$ -ray yields  $Y_\gamma^{\text{obs}}$  are listed in Table I. The values of  $Y_\gamma^{\text{obs}}$  are the weighted averages of the yields obtained from the Ge1 and Ge2 data (in all cases the Ge1 and Ge2 yields were consistent). It is important to note

TABLE I. The 22 observed  $\gamma$ -rays from isotopes of Ne and F produced in  $\mu^-$  capture on  $^{23}\text{Na}$ . The  $\gamma$ -ray yields  $Y_\gamma^{\text{obs}}$  include both direct and indirect capture, and they are per muon stop not per muon capture.

Product	$E_i$ (keV)	$J_i^\pi$	$E_f$ (keV)	$J_f^\pi$	$E_\gamma$ (keV)	$Y_\gamma^{\text{obs}} (\times 10^{-2})$
$^{23}\text{Ne}$	1017	$1/2^+$	0	$5/2^+$	1017	$1.24 \pm 0.28$
$^{23}\text{Ne}$	1702	$7/2^+$	0	$5/2^+$	1702	$0.17 \pm 0.04$
$^{23}\text{Ne}$	1823	$3/2^+$	0	$5/2^+$	1823	$1.43 \pm 0.30$
$^{23}\text{Ne}$	2315	$5/2^+$	1823	$3/2^+$	492	$0.12 \pm 0.04$
$^{23}\text{Ne}$	2315	$5/2^+$	0	$5/2^+$	2315	$0.13 \pm 0.04$
$^{23}\text{Ne}$	3432	$3/2^+$	1017	$1/2^+$	2415	$0.17 \pm 0.04$
$^{23}\text{Ne}$	3432	$3/2^+$	0	$5/2^+$	3432	$0.26 \pm 0.05$
$^{23}\text{Ne}$	3458	$1/2^+$	1823	$3/2^+$	1635	$0.79 \pm 0.17$
$^{23}\text{Ne}$	3458	$1/2^+$	1017	$1/2^+$	2441	$0.46 \pm 0.10$
$^{22}\text{Ne}$	1274	$2^+$	0	$0^+$	1274	$23.0 \pm 5.2$
$^{22}\text{Ne}$	3357	$4^+$	1274	$2^+$	2083	$2.95 \pm 0.61$
$^{22}\text{Ne}$	4457	$2^+$	1274	$2^+$	3183	$3.77 \pm 0.77$
$^{22}\text{Ne}$	5147	$2^-$	4457	$2^+$	690	$0.61 \pm 0.20$
$^{22}\text{Ne}$	5147	$2^-$	1274	$2^+$	3873	$0.66 \pm 0.15$
$^{22}\text{Ne}$	5523	$4^+$	3357	$4^+$	2166	$0.25 \pm 0.05$
$^{22}\text{Ne}$	5641	$3^+$	3357	$4^+$	2284	$0.17 \pm 0.04$
$^{21}\text{Ne}$	1746	$7/2^+$	351	$5/2^+$	1395	$0.73 \pm 0.16$
$^{21}\text{Ne}$	2789	$1/2^-$	351	$5/2^+$	2438	$0.32 \pm 0.07$
$^{21}\text{Ne}$	2789	$1/2^-$	0	$3/2^+$	2789	$0.06 \pm 0.01$
$^{20}\text{Ne}$	1634	$3^+$	0	$0^+$	1634	$0.48 \pm 0.10$
$^{20}\text{F}$	656	$3^+$	0	$2^+$	656	$0.13 \pm 0.03$
$^{20}\text{F}$	823	$4^+$	0	$2^+$	823	$0.06 \pm 0.01$

that the values of  $Y_\gamma^{\text{obs}}$  are  $\gamma$ -ray yields per muon stop not per muon capture, include both direct and indirect production of the  $\gamma$  ray's parent state, and correspond to the experimental mixture of  $F_+$  and  $F_-$  states. The quoted errors in the yields include the statistical uncertainties in  $N_\gamma$  and the uncertainties in the acceptances and various correction factors.

### B. State yields from $\mu^-$ capture on $^{23}\text{Na}$

The 22  $\gamma$  rays correspond to 17 states in the various Ne and F isotopes with six states in  $^{23}\text{Ne}$  and  $^{22}\text{Ne}$ , two states in  $^{21}\text{Ne}$  and  $^{20}\text{F}$ , and one state in  $^{20}\text{Ne}$ . The yields of these states were calculated using the equation

$$Y_S^{\text{obs}} = \sum_j Y_\gamma^{\text{obs}}(j)/f_{\text{br}} - \sum_k Y_\gamma^{\text{obs}}(k) \quad (7)$$

where the summation over  $j$  represents the sum of the yields for the  $\gamma$  rays from the state of interest and the summation over  $k$  represents the sum of the yields for the  $\gamma$ -rays feeding the state of interest. The subtraction of the term  $\sum Y_\gamma^{\text{obs}}(k)$  from the term  $\sum Y_\gamma^{\text{obs}}(j)$  in Eq. (7) means the quantity  $Y_S^{\text{obs}}$  represents the direct  $\mu^-$  capture yield. The factor  $f_{\text{br}}$  in Eq. (7) corrects for any unobserved  $\gamma$ -ray branches from the state of interest. It is given by  $f_{\text{br}} = \sum \text{br}(j)$  — the sum of the branching ratios of the observed  $\gamma$  rays — and was calculated using the branching ratio compilations of Endt [49].

The state yields  $Y_S^{\text{obs}}$  for the 17 states, calculated from the  $\gamma$ -ray yields  $Y_\gamma^{\text{obs}}$  in Table I using Eq. (7), are listed in Table II. The values of  $Y_S^{\text{obs}}$  are averages of the Ge1 and Ge2 data and the quoted errors include the statistical uncertainties in  $N_\gamma$ , and the uncertainties in the acceptances, various correction factors, and the branching ratios. In some cases, where the state is strongly populated such as the 1274 keV level in  $^{22}\text{Ne}$ , the uncertainties are dominated by the  $\sim 20\%$  overall normalization uncertainty. In other cases, where there is considerable feeding such as the 656 keV level in  $^{20}\text{F}$  [i.e., where  $\sum Y_\gamma^{\text{obs}}(k)$  and  $\sum Y_\gamma^{\text{obs}}(j)/f_{\text{br}}$  are comparable], the uncertainties are much larger.

### C. Parentage of states in muon capture on $^{23}\text{Na}$

In the interpretation of the hyperfine dependence data (Sec. V D) it is essential to know the parentage of each state. By parentage we mean what fraction of the state's population is due to direct  $\mu^-$  capture and what fraction of the state's population is due to indirect  $\mu^-$  capture via a higher energy state. We will denote the state of interest by  $S$  and the higher energy state by  $S'$ .

The parentage of state  $S$  due to direct  $\mu^-$  capture ( $P_S^S$ ) was obtained using the equation

$$P_S^S = \frac{Y_S^{\text{obs}}}{\sum Y_\gamma^{\text{obs}}(j)/f_{\text{br}}}, \quad (8)$$

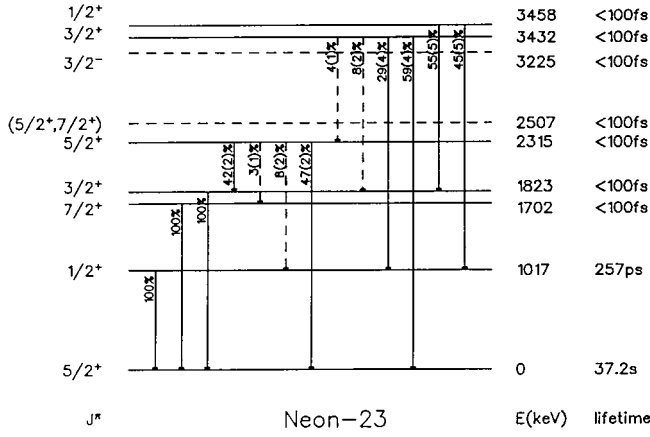


FIG. 4. Energy level diagram for the low-lying levels of  $^{23}\text{Ne}$  showing the nine  $\gamma$  rays and six states observed following muon capture on  $^{23}\text{Na}$ . The solid vertical lines correspond to the observed  $\gamma$ -ray branches and the dashed vertical lines correspond to the unobserved  $\gamma$ -ray branches. The spin parities, energies, lifetimes, and branching ratios are from the tabulations of Endt [49].

where  $\Sigma Y'_\gamma(j)/f_{\text{br}}$  is the yield of state  $S$  due to both direct and indirect capture and  $Y_S^{\text{obs}}$  is the yield of state  $S$  due to direct capture only. The parentage of state  $S$  due to indirect  $\mu^-$  capture via state  $S'$  ( $P_S^{S'}$ ) was obtained using the equation

$$P_S^{S'} = \frac{P_{S'}^{S'} Y'_\gamma^{\text{obs}}}{\Sigma Y'_\gamma^{\text{obs}}(j)/f_{\text{br}}} + f_{\text{ms}}, \quad (9)$$

where in the denominator  $\Sigma Y'_\gamma^{\text{obs}}(j)/f_{\text{br}}$  is the yield of  $S$  due to direct and indirect capture, in the numerator  $Y'_\gamma^{\text{obs}}$  is the  $\gamma$ -ray yield for the transition from the state  $S'$  to the state  $S$ , and  $P_{S'}^{S'}$  is the parentage of state  $S'$  due to direct capture to state  $S'$ . The correction factor  $f_{\text{ms}}$  accounts for the population of the state  $S$  by the state  $S'$  via a multistep, rather than a single-step,  $\gamma$ -ray decay.

The state parentages, calculated using the values of  $Y'_\gamma^{\text{obs}}$  and  $Y_S^{\text{obs}}$  in Tables I and II using Eqs. (8) and (9), are listed in Table III. The values of  $P_S^S$  and  $P_S^{S'}$  are averages of the Ge1 and Ge2 data and the quoted errors include the statistical uncertainties in  $N_\gamma$  and the uncertainties in the acceptances, various correction factors, and branching ratios. Table III indicates, for example, the parentage of the 1017 keV state in  $^{23}\text{Ne}$  is  $(47 \pm 3)\%$  due to direct capture to the  $^{23}\text{Ne}$  1017 keV state and  $(2 \pm 1)\%$ ,  $(15 \pm 2)\%$ , and  $(37 \pm 5)\%$  due to indirect capture via the  $^{23}\text{Ne}$  2315, 3432, and 3458 keV states, respectively.

#### D. $\gamma$ -ray hyperfine dependences from $\mu^-$ capture on $^{23}\text{Na}$

In the presence of hyperfine transitions the time dependence of  $\gamma$  rays from muon capture is given by

$$Y'_\gamma(t) = A e^{-\Lambda_D t} (1 + k e^{-\Lambda_h t}), \quad (10)$$

with

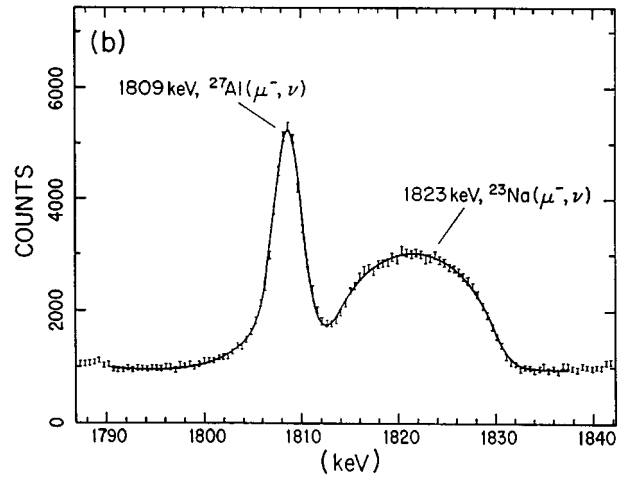
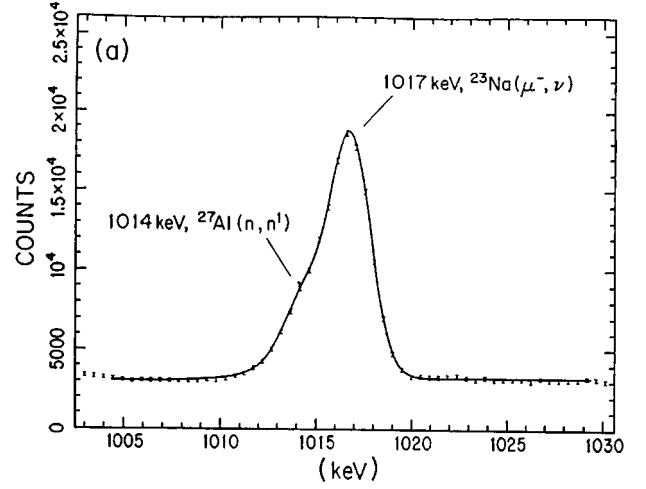


FIG. 5. The Ge1 energy spectra in the region of (a) the 1017 keV  $\gamma$ -ray and (b) the 1823 keV  $\gamma$  ray following muon capture on  $^{23}\text{Na}$ . The points are the experimental data and the solid lines are the “best fits” using the measured energy resolution functions. The energy spectra also show background lines from the  $(n, n')$  and  $(\mu^-, \nu)$  reactions on aluminum (see Ref. [26] for more details).

$$k = f_+ (Y'_\gamma^+ / Y'_\gamma^- - 1), \quad (11)$$

where  $A$  is an arbitrary normalization factor,  $\Lambda_D$  is the muon disappearance rate,  $\Lambda_h$  is the hyperfine transition (HF) rate,  $f_+$  is the initial population of the  $F_+$  hyperfine state, and  $Y'_\gamma^+ / Y'_\gamma^-$  is the hyperfine dependence of the  $\gamma$ -ray yield. Equations (10) and (11) assume the difference in the disappearance rates from the two HF states,  $\delta\Lambda_D = \Lambda_{D-} - \Lambda_{D+}$ , is much smaller than  $\Lambda_h$ , which is the case in  $^{23}\text{Na}$  ( $\delta\Lambda_D / \Lambda_h \sim 0.004$  [39,50]). We also assume that the two HF states are initially statistically populated, i.e.,  $f_+ = (J_i + 1) / (2J_i + 1)$ . Effects leading to a nonstatistical population at  $t=0$ , for example  $M1$  transitions in the  $\mu^-$  atomic cascade, were examined by Congleton [34] and are expected to be negligible in muonic  $^{23}\text{Na}$ .

Based on Eqs. (10) and (11) the hyperfine dependence of the  $\gamma$ -ray yields  $Y'_\gamma^+ / Y'_\gamma^-$  can be extracted from the  $\gamma$ -ray time dependence  $Y'_\gamma(t)$ . In turn, these  $\gamma$ -ray hyperfine dependences carry their parent state's hyperfine dependence, i.e.,  $Y'_\gamma^+ / Y'_\gamma^- = Y_S^+ / Y_S^-$ .

TABLE II. State yields, capture rates, and hyperfine dependences corresponding to the 17 observed states in Ne and F isotopes following  $\mu^-$  capture on  $^{23}\text{Na}$ . The state yields  $Y_S^{\text{obs}}$  and capture rates  $\Lambda_S^{\text{obs}}$  include direct capture only. The hyperfine dependences  $Y_S^{'+}/Y_S'^{-} = \Lambda_S^{'+}/\Lambda_S'^{-}$  include both direct and indirect capture and are weighted averages of the hyperfine dependences of all  $\gamma$ -rays emitted by the particular parent state.

Product	$E_f$ (keV)	$J_f^\pi$	$Y_S^{\text{obs}} (\times 10^{-2})$	$\Lambda_S^{\text{obs}} (\times 10^3 \text{ s}^{-1})$	$Y_S^{'+}/Y_S'^{-} = \Lambda_S^{'+}/\Lambda_S'^{-}$
$^{23}\text{Ne}$	1017	$1/2^+$	$0.59 \pm 0.17$	$4.9 \pm 1.4$	$0.18 \pm 0.03$
$^{23}\text{Ne}$	1702	$7/2^+$	$0.16 \pm 0.04$	$1.4 \pm 0.3$	$\leq 0.50$
$^{23}\text{Ne}$	1823	$3/2^+$	$0.49 \pm 0.11$	$4.1 \pm 0.9$	$0.23 \pm 0.04$
$^{23}\text{Ne}$	2315	$5/2^+$	$0.26 \pm 0.06$	$2.1 \pm 0.5$	$0.87 \pm 0.48$
$^{23}\text{Ne}$	3432	$3/2^+$	$0.49 \pm 0.10$	$4.1 \pm 0.8$	$0.98 \pm 0.36$
$^{23}\text{Ne}$	3458	$1/2^+$	$1.25 \pm 0.26$	$10.4 \pm 2.2$	$\leq 0.19$
$^{22}\text{Ne}$	1274	$2^+$	$16.0 \pm 3.7$	$133 \pm 31$	$0.88 \pm 0.07$
$^{22}\text{Ne}$	3357	$4^+$	$2.52 \pm 0.52$	$21 \pm 4$	$1.97 \pm 0.06$
$^{22}\text{Ne}$	4457	$2^+$	$3.28 \pm 0.67$	$27 \pm 6$	$1.00 \pm 0.08$
$^{22}\text{Ne}$	5147	$2^-$	$1.28 \pm 0.31$	$11 \pm 3$	$0.41 \pm 0.17$
$^{22}\text{Ne}$	5523	$4^+$	$0.25 \pm 0.05$	$2.1 \pm 0.4$	$2.27 \pm 0.38$
$^{22}\text{Ne}$	5641	$3^+$	$0.60 \pm 0.14$	$5.0 \pm 1.1$	$\leq 1.2$
$^{21}\text{Ne}$	1746	$7/2^+$	$0.77 \pm 0.17$	$6.4 \pm 1.4$	$1.32 \pm 0.14$
$^{21}\text{Ne}$	2789	$1/2^-$	$0.38 \pm 0.08$	$3.2 \pm 0.7$	$0.64 \pm 0.15$
$^{20}\text{Ne}$	1634	$3^+$	$0.48 \pm 0.10$	$4.0 \pm 0.8$	$0.93 \pm 0.14$
$^{20}\text{F}$	656	$3^+$	$0.03 \pm 0.02$	$0.2 \pm 0.2$	$0.79 \pm 0.19$
$^{20}\text{F}$	823	$4^+$	$0.16 \pm 0.04$	$1.3 \pm 0.3$	$\leq 1.6$

Two methods (denoted A and B) were used to extract values of  $Y_\gamma^{'+}/Y_\gamma'^{-}$  and therefore  $Y_S^{'+}/Y_S'^{-}$  from the  $\gamma$ -ray time spectra. In method A, 120 time-binned energy spectra were generated corresponding to  $\sim 10$  ns wide bins from  $t = -100$  to  $+1100$  ns. Fits to the  $\gamma$ -ray peaks in each time-binned energy spectrum were then performed to determine the  $\gamma$ -ray time spectra  $Y_\gamma'(t)$ . Finally, fits to the  $\gamma$ -ray time spectra, using the theoretical time dependence of Eqs. (10) and (11) convoluted with the time resolution functions  $R_1(t)$  and  $R_2(t)$ , were used to extract  $Y_\gamma^{'+}/Y_\gamma'^{-}$  and  $\Lambda_h$ . The weighted average of the values of  $\Lambda_h$  was  $15.5 \pm 1.1 \mu\text{s}^{-1}$  and has been discussed in Ref. [26]. Representative  $\gamma$ -ray time spectra, illustrating the quality of the data, are shown in Fig. 6.

In method B the  $\gamma$ -ray energy spectra were divided into two time windows, an early time window with  $t=0$  to 170 ns, and a late time window with  $t=200$  to 1000 ns. For the case of  $\mu^-^{23}\text{Na}$ , where  $\Lambda_h = 15.5 \pm 1.1 \mu\text{s}^{-1}$ , the early (late) time windows correspond to periods of significant (insignificant)  $F_+$  HF state population. The ratio of  $\gamma$ -ray counts in the early and late windows,  $R$ , is therefore a function of  $Y_\gamma^{'+}/Y_\gamma'^{-}$ . The values of  $R$  were obtained from fits to the  $\gamma$ -ray peaks in the corresponding early and late energy spectra. The  $\gamma$ -ray hyperfine dependence  $Y_\gamma^{'+}/Y_\gamma'^{-}$  was then extracted from  $R$  using a Monte Carlo simulation that determined the relationship between  $Y_\gamma^{'+}/Y_\gamma'^{-}$  and  $R$  (we used a Monte Carlo simulation because of the complications of the updating  $\mu\text{STOP}$  logic and  $\mu^-$  pileup). The method required values of  $\Lambda_D$  and  $\Lambda_h$  as input; we took  $\Lambda_D = 8.31 \pm 0.02 \mu\text{s}$  from Suzuki *et al.* [51] and  $\Lambda_h = 15.5 \pm 1.1 \mu\text{s}^{-1}$  extracted from method A.

For the stronger  $\gamma$ -rays transitions at the energies of 1017, 1274, 1823, and 2127 keV it was feasible to use both methods A and B to extract  $Y_\gamma^{'+}/Y_\gamma'^{-}$  while for the weaker  $\gamma$ -rays transitions only method B was practical. Where both methods were feasible they were consistent. The results of the determinations of the  $\gamma$ -ray hyperfine dependences are listed in Table II (where method A was used we quote the method A results). We quote the state hyperfine dependences  $Y_S^{'+}/Y_S'^{-}$  that are the weighted averages of  $\gamma$ -ray hyperfine dependences  $Y_\gamma^{'+}/Y_\gamma'^{-}$  that decay from the same parent state. In all cases the  $\gamma$ -ray hyperfine dependences  $Y_\gamma^{'+}/Y_\gamma'^{-}$  corresponding to the same parent state were in mutual agreement. The results are the weighted averages of the Ge1 and Ge2 data and the quoted errors include the statistical uncertainties in  $Y_\gamma'(t)$ , the uncertainties in  $R_1(t)$  and  $R_2(t)$ , and the correlations of  $Y_\gamma^{'+}/Y_\gamma'^{-}$  with  $\Lambda_h$  and  $\Lambda_D$ .

To test for distortions of the  $\gamma$ -ray time spectra we also fitted the time spectra of events following  $\mu^-$  stops in targets of Ca, Fe, and Pb. In the Ca, Fe, and Pb targets the muon lifetime ranges from 78 to 330 ns (see Ref. [51]) and there is no observable hyperfine effect. Good fits were obtained using a prompt x-ray peak and a single exponential with the appropriate muon lifetime.

Lastly, the weighted mean of the values of  $\Lambda_h$  extracted from the 1017, 1823, and 2127 keV  $\gamma$ -ray time spectra with method A, and the assumption of initially statistically populated  $F_-$  and  $F_+$  hyperfine states, were used to determine the fractional population of the  $F_-$  and  $F_+$  states in the experimental  $2.0 \mu\text{s}$   $\mu\text{STOP}$  gate. We obtained fractional populations of 0.97 and 0.03 for the  $F_-$  and  $F_+$  hyperfine states,

TABLE III. The measured parentage  $P_S^{S'}$  of the various Ne and F states produced in  $\mu^-$  capture on  $^{23}\text{Na}$ . The states  $S$  and  $S'$ , defined in the text, correspond to rows and columns, respectively. As an example the parentage of the 1017 keV state in  $^{23}\text{Ne}$  is (47±3)% direct capture to the 1017 keV state and (37±5)%, (15±2)%, and (2±1)% indirect capture via the 3458, 3432, and 2315 keV states, respectively.

$E_f$						
$^{23}\text{Ne}$	3458, 1/2 <sup>+</sup>	3432, 3/2 <sup>+</sup>	2315, 5/2 <sup>+</sup>	1823, 3/2 <sup>+</sup>	1702, 7/2 <sup>+</sup>	1017, 1/2 <sup>+</sup>
3458	1.00					
3432		1.00				
2315		0.07±0.02	0.93±0.02			
1823	0.55±0.01	0.03±0.01	0.08±0.02	0.34±0.01		
1702		0.05±0.02			0.96±0.01	
1017	0.37±0.05	0.15±0.02	0.02±0.01			0.47±0.03
$^{22}\text{Ne}$	5641, 4 <sup>+</sup>	5523, 3 <sup>+</sup>	5147, 2 <sup>-</sup>	4457, 2 <sup>+</sup>	3357, 4 <sup>+</sup>	1274, 2 <sup>+</sup>
5641	1.00					
5523		1.00				
5147			1.00			
4457			0.15±0.05	0.85±0.05		
3357	0.06±0.01	0.09±0.01			0.86±0.01	
1274	0.03±0.01	0.01±0.01	0.05±0.01	0.13±0.02	0.11±0.01	0.67±0.03
$^{21}\text{Ne}$	2789, 1/2 <sup>-</sup>	1746, 7/2 <sup>+</sup>				
2789	1.00					
1746		1.00				
$^{20}\text{Ne}$	1634, 3 <sup>+</sup>					
1634	1.00					
$^{20}\text{F}$	823, 4 <sup>+</sup>	656, 3 <sup>+</sup>				
823	1.00					
656	0.78±0.10	0.22±0.10				

respectively. Yields and capture rates measured in the 2.0  $\mu\text{s}$   $\mu\text{STOP}$  gate were therefore related to the  $F_-$  and  $F_+$  hyperfine state yields and capture rates by  $Y^{\text{obs}} = 0.97Y^- + 0.03Y^+$  and  $\Lambda^{\text{obs}} = 0.97\Lambda^- + 0.03\Lambda^+$ .

## VI. INTERPRETATION OF THE $\mu^-^{23}\text{Na}$ DATA

### A. Formulas for nuclear muon capture

A number of authors have published formulas for muon capture rates and their hyperfine dependences (for example Refs. [27,52,53]). Using Walecka's notation [52] the  $\mu^-$  capture rate from a statistical mixture of  $F_+$  and  $F_-$  hyperfine states is

$$\Lambda^{\text{stat}} = \frac{G^2 \nu^2}{2\pi(1+\nu/M)} \frac{4\pi}{2J_i+1} \left\{ \sum_{J=0}^{\infty} |\langle J_f || \hat{\mathcal{L}}_J - \hat{\mathcal{M}}_J || J_i \rangle|^2 + \sum_{J=1}^{\infty} |\langle J_f || \hat{\mathcal{T}}_J^{\text{el}} - \hat{\mathcal{T}}_J^{\text{mag}} || J_i \rangle|^2 \right\} |\phi_{1s}|_{\text{av}}^2, \quad (12)$$

and the hyperfine increment  $\delta\Lambda^F$ , which determines the  $\mu^-$  capture rates from the individual  $F_+$  and  $F_-$  hyperfine

states via  $\Lambda^F = \Lambda^{\text{stat}} + \delta\Lambda^F$ , is

$$\begin{aligned} \delta\Lambda^F = & \frac{2\sqrt{2}G^2\nu^2}{(1+\nu/M)} (-1)^{F-J_f+(3/2)} \begin{Bmatrix} J_i & \frac{1}{2} & F \\ \frac{1}{2} & J_i & 1 \end{Bmatrix} \\ & \times \sum_J \sum_{J'} \sqrt{(2J+1)(2J'+1)} \begin{Bmatrix} J_i & J & J_f \\ J' & J_i & 1 \end{Bmatrix} \\ & \times [i^{J-J'} \langle J_f || \hat{\mathcal{L}}_J - \hat{\mathcal{M}}_J || J_i \rangle \langle J_f || \hat{\mathcal{L}}_{J'} - \hat{\mathcal{M}}_{J'} || J_i \rangle^* \\ & \times \langle J0J'0 | 10 \rangle + i^{J-J'} \langle J_f || \hat{\mathcal{T}}_J^{\text{el}} - \hat{\mathcal{T}}_J^{\text{mag}} || J_i \rangle \\ & \times \langle J_f || \hat{\mathcal{T}}_{J'}^{\text{el}} - \hat{\mathcal{T}}_{J'}^{\text{mag}} || J_i \rangle^* \langle J1J' - 1 | 10 \rangle \\ & + 2\sqrt{2}\Re(i^{J-J'} \langle J_f || \hat{\mathcal{L}}_J - \hat{\mathcal{M}}_J || J_i \rangle \langle J_f || \hat{\mathcal{T}}_{J'}^{\text{el}} - \hat{\mathcal{T}}_{J'}^{\text{mag}} || J_i \rangle \\ & \times \langle J1J'0 | 11 \rangle)]. \end{aligned} \quad (13)$$

In these equations  $G$  is the universal weak coupling constant,  $\nu$  is the neutrino momentum,  $\phi_{1s}$  is the muon wave function at the nucleus, and  $\mathcal{L}_J$ ,  $\mathcal{M}_J$ ,  $\mathcal{T}_J^{\text{el}}$ , and  $\mathcal{T}_J^{\text{mag}}$  are the so-called longitudinal, charge, transverse electric, and transverse mag-

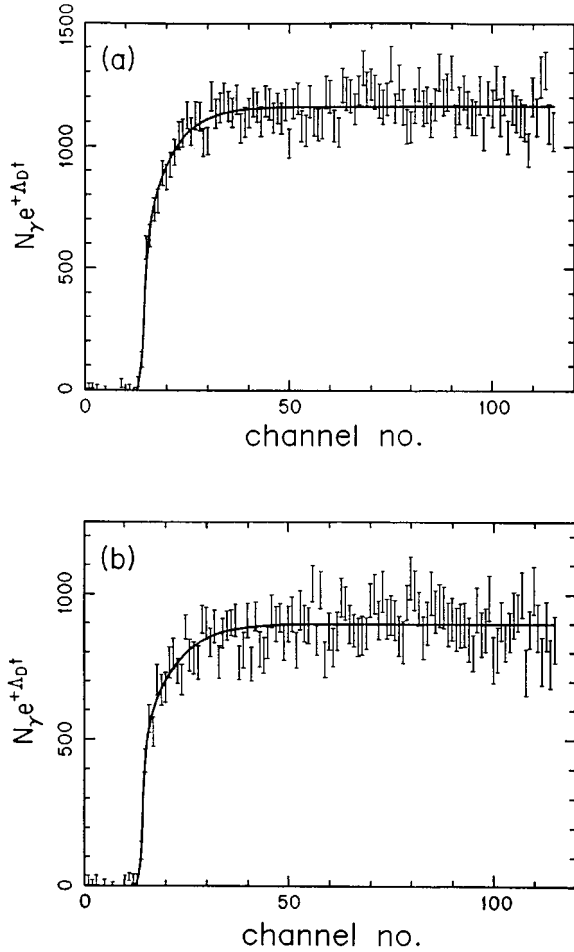


FIG. 6. The Ge2 time spectra of (a) the 1017 keV  $\gamma$  ray and (b) the 1823 keV  $\gamma$  ray following muon capture on  $^{23}\text{Na}$ . The points are the experimental data and the solid lines are the theoretical time distributions convoluted with the measured time resolution functions. We have divided out the  $\mu^-$  disappearance rate to more clearly show the  $\mu^-$  hyperfine effect. The calibration is 9.58 ns per channel.

netic operators. In deducing Eqs. (12) and (13) it is assumed the muon wave function is constant over the nuclear volume.

In general the operators  $\mathcal{L}_J$ ,  $\mathcal{M}_J$ ,  $\mathcal{T}_J^{\text{el}}$ , and  $\mathcal{T}_J^{\text{mag}}$  contain contributions from one-, two- and many-body weak nucleonic currents. However, in this paper, we will assume that these operators can be represented by the sum of  $A$  one-body weak nucleonic currents, and that the effects of two- through  $A$ -body currents can be incorporated by replacing the free coupling constants by effective coupling constants (e.g.,  $g_p$  by  $\tilde{g}_p$ ). In such circumstances the nuclear matrix elements of  $\mathcal{L}_J$ ,  $\mathcal{M}_J$ ,  $\mathcal{T}_J^{\text{el}}$ , and  $\mathcal{T}_J^{\text{mag}}$  can be written as sums of products of single-particle matrix elements (SPME's) and one-body transition densities (OBTD's) where the SPME's contain all the weak interaction information and the OBTD's contain all the nuclear structure information.

The  $\mathcal{L}_J$ ,  $\mathcal{M}_J$ ,  $\mathcal{T}_J^{\text{el}}$ , and  $\mathcal{T}_J^{\text{mag}}$  SPME's, assuming their one-body form, can be expressed as combinations of the weak nucleon form factors and SPME's of the four multipole operators  $M_J^M$ ,  $M_{JL}^M \cdot \sigma$ ,  $M_{JL}^M \cdot \nabla$ , and  $M_J^M \sigma \cdot \nabla$ , where the functions  $M_J^M$  and  $M_{JL}^M$  are products of spherical Bessel functions

$j_J(qx)$  and spherical and vector spherical harmonics  $Y_J^M$  and  $\mathcal{Y}_{JL}^M$

$$M_J^M \equiv j_J(qx) Y_J^M(\theta, \phi), \quad (14)$$

$$M_{JL}^M \equiv j_L(qx) \mathcal{Y}_{JL}^M(\theta, \phi). \quad (15)$$

In the case of harmonic oscillator wave functions the  $\mathcal{L}_J$ ,  $\mathcal{M}_J$ ,  $\mathcal{T}_J^{\text{el}}$ , and  $\mathcal{T}_J^{\text{mag}}$  SPME's can be evaluated analytically (for example see Donnelly and Haxton [54]).

The operators  $\mathcal{L}_1$  and  $\mathcal{T}_1^{\text{el}}$  are of special significance corresponding to, in the long wave length limit, the familiar Gamow-Teller operator (GT)

$$\mathcal{L}_1 = \frac{1}{\sqrt{2}} \mathcal{T}_1^{\text{el}} = \frac{i}{\sqrt{12\pi}} g_a \sum_{i=1}^A \sigma_i \tau_i^{\pm} \quad (16)$$

responsible for Gamow-Teller transitions.

### B. $^{23}\text{Na} \rightarrow ^{23}\text{Ne}$ shell model calculations

To calculate the OBTD's for the various  $^{23}\text{Na}(\mu^-, \nu) ^{23}\text{Ne}$  transitions we used the OXBASH shell-model computer code [55]. The calculations were performed in the  $1s-0d$  model space using two effective interactions; the empirical interaction of Brown and Wildenthal [56] (denoted USD) and the realistic interaction of Kuo and Brown [57] (denoted KUU). The two-body matrix elements of the USD interaction were obtained by Brown and Wildenthal from a fit to  $\sim 440$  energy levels of  $1s-0d$  shell nuclei. The two-body matrix elements of the KUU interaction were obtained by Kuo and Brown from the Hamada-Johnson nucleon-nucleon potential [58]. In the following calculations we used an oscillator parameter  $b$  of 1.804 fm and single-particle energies of  $-3.948$ ,  $-3.164$ , and  $+1.647$  MeV for the  $0d_{5/2}$ ,  $1s_{1/2}$ , and  $0d_{3/2}$  orbitals, respectively.

Figure 7 is a comparison of the measured energy levels with the KUU and USD calculated energy levels for  $^{23}\text{Ne}$ . In the case of the USD interaction Fig. 7 shows good agreement between the experimental and theoretical low-lying positive parity states with an r.m.s. deviation between the measured and calculated energy levels of  $\sim 40$  keV. The good agreement suggests identification of the 2507 keV experimental state with the  $9/2^+$  model state. In the case of the KUU interaction Fig. 7 shows, at first glance, poor agreement between the measured and calculated energy levels. However, a means of reconciling the measured and calculated levels has been suggested by Cole *et al.* [59]. Based on the calculated quadrupole moments they identified the  $5/2_1^+$ ,  $7/2_2^+$ , and  $9/2_2^+$  model states as members of a  $K=5/2^+$  rotational band and the  $1/2_1^+$ ,  $3/2_1^+$ , and  $5/2_2^+$  model states as members of a  $K=1/2^+$  rotational band and by a  $\sim 2$  MeV downward shift of the  $K=5/2^+$  band relative to the  $K=1/2^+$  band. Cole *et al.* obtained good agreement between the experimental and theoretical energy levels (see Fig. 7). Apparently, the KUU interaction does a relatively good job for the energy spacing of states within a rotational band, but a relatively poor job for the energy spacing of the rotational band heads.

We conclude, therefore, that the  $1s-0d$  shell-model calculations, using either the USD and KUU effective interactions, yield sufficient agreement between the experimental



TABLE V. Results of the fits of the calculated and measured  $\mu^-$  capture rates and hyperfine dependences for the six  $^{23}\text{Na} \rightarrow ^{23}\text{Ne}^*$  transitions using the  $1s-0d$  shell model and the KUO realistic effective interaction. The “best fit” value of  $\tilde{g}_a$  is  $-1.34 \pm 0.09$  and the “best fit” value of  $\tilde{g}_p/\tilde{g}_a$  is  $7.9 \pm 2.2$ . Note the capture rates  $\Lambda_S^{\text{obs}}$  include direct capture only whereas the hyperfine dependences  $Y_S^+/Y_S'^- = \Lambda_S^+/\Lambda_S'^-$  include both direct and indirect capture.

$E_f$ (keV)	$J_f^\pi$	$\Lambda_S^{\text{obs}} (\times 10^3 \text{ s}^{-1})$		$Y_S^+/Y_S'^- = \Lambda_S^+/\Lambda_S'^-$	
		expt.	calc.	expt.	calc.
1017	$1/2^+$	$4.9 \pm 1.4$	4.96	$0.18 \pm 0.03$	0.18
1702	$7/2^+$	$1.4 \pm 0.3$	0.11	$\leq 0.50$	0.49
1823	$3/2^+$	$4.1 \pm 0.9$	5.96	$0.23 \pm 0.04$	0.16
2315	$5/2^+$	$2.1 \pm 0.5$	0.64	$0.98 \pm 0.36$	0.23
3432	$3/2^+$	$4.1 \pm 0.8$	2.61	$0.87 \pm 0.48$	0.44
3458	$1/2^+$	$10.4 \pm 2.2$	8.22	$\leq 0.19$	0.13

extracted from previous  $\beta^-/\beta^+$ -decay and  $(p,n)/(n,p)$  charge exchange data using the USD interaction (see for example [60]). The  $\sim 30\%$  difference in the values of  $\tilde{g}_a$  extracted from the KUO and USD calculations is due to systematically smaller GT matrix elements in the KUO computation compared to the USD computation. Systematic differences between the empirical USD interaction and realistic KUO interaction are not surprising — they are philosophically distinctly different interactions — and it highlights the fact that one quotes effective couplings in the context of an effective interaction. Such systematic differences have been reported by Jiang *et al.* [61].

Unlike the 1017, 1823, 3432, and 3458 keV transitions, the measured and calculated  $\mu^-$  capture rates for the weak 1702 and 2315 keV transitions do not agree quantitatively. The reason is suggested by Table VI, which compares the calculated  $\mu^-$  capture rates using (i) all nuclear matrix elements, and (ii) only GT nuclear matrix elements. While the 1017, 1823, 3432, and 3458 keV transitions, where experiment and theory agree well, are dominated by the GT matrix element, the 1702 and 2315 keV transitions, where experiment and theory agree less well, have little or no contribution from the GT matrix element.

An examination of the KUO and USD calculations for the 2315 keV transition shows it is dominated by the spin-quadrupole matrix element (i.e.,  $M_{J2} \cdot \sigma$ ) rather than the Gamow-Teller matrix element (i.e.,  $M_{01} \cdot \sigma$ ). Spin-quadrupole matrix elements have been examined via second-forbidden unique  $\beta$  decay. However, Warburton [62], using the  $1s-0d$  shell model and USD interaction, found theoretic

cal rates consistently larger than experimental rates for second-forbidden unique  $\beta$  decay — the reverse of the 2315 keV transition case. It would be speculative to draw conclusions on the difference between the  $M_{J2} \cdot \sigma$  matrix element in  $\mu^-$  capture and  $\beta$  decay based on one  $\mu^-$  capture transition and a few  $\beta$ -decay transitions, but, it does suggest that while the  $1s-0d$  shell model with USD interaction does a good job in reproducing the Gamow-Teller matrix elements, it does a poorer job in reproducing the spin-quadrupole matrix elements.

The only significant difference between the USD calculation with  $\tilde{g}_a = -1.01$  and the KUO calculation with  $\tilde{g}_a = -1.34$  is the 1702 keV transition where the capture rates are  $6.4 \times 10^2 \text{ s}^{-1}$  and  $1.1 \times 10^2 \text{ s}^{-1}$ , respectively, a factor of  $\sim 6$  difference. An inspection of the KUO and USD interaction OBTD's for the 1702 keV transition indicate the dominant  $0d_{5/2} \rightarrow 0d_{5/2}$  OBTD is considerably larger in the USD calculation (0.51) than the KUO calculation (0.27). Additionally, the r.m.s. value of the other OBTD's are  $\sim 0.09$  in both the KUO and USD cases, and consequently there is more interference between the dominant  $0d_{5/2} \rightarrow 0d_{5/2}$  single-particle transition and other single-particle transitions in the KUO calculation than in the USD calculation. This is the origin of the very different 1702 keV  $\mu^-$  capture rates in the KUO and USD calculations.

In summary, the comparisons of the KUO and USD calculations with the observed  $\mu^-$  capture rates indicate the high quality of the model calculations of GT matrix elements for the strong and intermediate 1017, 1823, 3432, and 3458

TABLE VI. Comparison of the  $\mu^-$  capture rates calculated using (i) all nuclear matrix elements, and (ii) only Gamow-Teller nuclear matrix elements. Results employing both the USD effective effective interaction and the KUO realistic effective interaction are listed.

$E_f$ (keV)	$J_f^\pi$	$\Lambda_S^{\text{obs}} (\times 10^3 \text{ s}^{-1})$		$\Lambda_S^{\text{obs}} (\times 10^3 \text{ s}^{-1})$	
		USD (GT only)	USD	KUO (GT only)	KUO
1017	$1/2^+$	4.81	5.26	4.72	4.96
1702	$7/2^+$	0.00	0.64	0.00	0.11
1823	$3/2^+$	3.62	6.28	2.96	5.96
2315	$5/2^+$	0.06	0.71	0.10	0.64
3432	$3/2^+$	2.44	2.40	3.35	2.61
3458	$1/2^+$	10.74	8.97	11.54	8.22

TABLE VII. Comparison of the Gamow-Teller transition probabilities ( $B_{\text{GT}}$ ) of Siebels *et al.* [63], extracted from measurements of the  $^{23}\text{Na}(n,p)^{23}\text{Ne}^*$  reaction at forward angles and medium energies, with  $1s-0d$  shell model calculations using the USD empirical effective interaction [56] and KUO realistic effective interaction [57]. A  $B_{\text{GT}}$  sum is quoted for the 3432 and 3458 keV transitions as they are unresolved in the  $(n,p)$  experiment.

$E_f$ (keV)	$J_f^\pi$	$B_{\text{GT}}$ (Expt.)	$B_{\text{GT}}$ (USD)	$B_{\text{GT}}$ (KUO)
0	$5/2^+$	$0.038 \pm 0.006$	0.026	0.054
1017	$1/2^+$	$0.048 \pm 0.007$	0.111	0.123
1823	$3/2^+$	$0.041 \pm 0.008$	0.130	0.120
2315	$5/2^+$	$\leq 0.021$	0.039	0.038
3432–3458	$3/2^+ - 1/2^+$	$0.318 \pm 0.033$	0.334	0.438

keV transitions, but some difficulties with the  $\ell = 2$  matrix elements and the weak 1702 and 2315 keV transitions. The agreement of the values of  $\tilde{g}_a$  extracted using the  $1s-0d$  shell model with USD interaction from our  $\mu^-$  capture data and previous  $\beta^+/\beta^-$  decay and  $(p,n)/(n,p)$  charge exchange data builds confidence in the model's application to muon capture on  $^{23}\text{Na}$ . The generally good agreement of the KUO and USD calculations with the  $\mu^-$  capture data, albeit with somewhat different ‘‘best fit’’ values of  $\tilde{g}_a$ , is additional evidence of the high quality of the nuclear models.

#### D. $B_{\text{GT}}$ values for the $^{23}\text{Na} \rightarrow ^{23}\text{Ne}$ Gamow-Teller transitions

As a further test of the nuclear model we have compared the KUO and USD calculations of GT transition probabilities with determinations of the GT transition probabilities via the  $(n,p)$  charge exchange reaction on  $^{23}\text{Na}$ . The  $(n,p)$  reaction at medium energies and forward angles is an established probe of GT transition probabilities ( $B_{\text{GT}}$ ) and Siebels *et al.* [63] have recently measured  $^{23}\text{Na}(n,p)^{23}\text{Ne}^*$  cross sections at medium energies and forward angles and extracted values of  $B_{\text{GT}}$  to a number of the low-lying  $^{23}\text{Ne}$  levels.

Values of  $B_{\text{GT}}$  defined by

$$B_{\text{GT}} = \frac{1}{2J_i + 1} \left| \left\langle J_f \left\| \sum_{i=1}^A \sigma_i \tau_i^\pm \right\| J_i \right\rangle \right|^2 \quad (17)$$

and obtained from the  $^{23}\text{Na}(n,p)$  data and the USD and KUO calculations are listed in Table VII. They include values of  $B_{\text{GT}}$  for the two lowest-lying  $1/2^+$  states (1017 and 3458 keV),  $3/2^+$  states (1823 and 3432 keV), and  $5/2^+$  states (g.s. and 2315 keV) in  $^{23}\text{Ne}$  (the non-GT 1702 keV transition is not included). In the case of the  $(n,p)$  data a  $B_{\text{GT}}$  sum is quoted for the 3432 and 3458 keV transitions [they are unresolvable in the  $(n,p)$  experiment] and a  $B_{\text{GT}}$  upper limit is quoted for the 2315 keV transition [it was unobserved in the  $(n,p)$  experiment]. Table VII shows agreement in the general distribution of  $B_{\text{GT}}$  strength obtained from the  $(n,p)$  experiment and KUO and USD calculations with strong transitions to the 3432–3458 keV doublet, intermediate transitions to the 1017 and 1823 keV states, and weak transitions to the g.s. and 2315 keV state. This builds additional confidence in the model calculations of the  $^{23}\text{Na} \rightarrow ^{23}\text{Ne}$  GT matrix elements. The ratio between the measured and calculated sum of  $B_{\text{GT}}$  values to the six

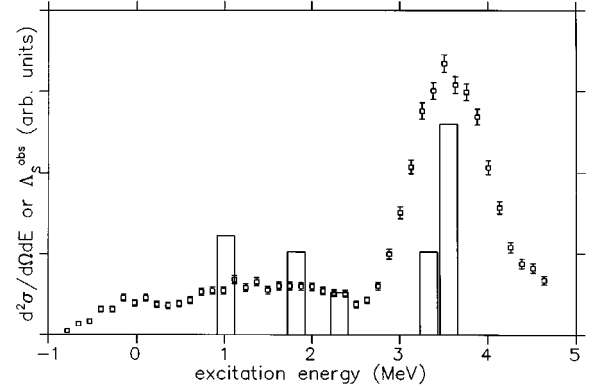


FIG. 8. Comparison of the  $^{23}\text{Na}(n,p) 0^\circ$  cross section measured by Siebels *et al.* [63] with the  $^{23}\text{Na}(\mu^-, \nu)^{23}\text{Ne}^*$  capture rate data. The points are the  $(n,p)$  data and the bars are the  $(\mu^-, \nu)$  data (the  $^{23}\text{Ne}$  levels are bound up to 5.193 MeV). The resemblance reflects the importance of the GT nuclear matrix elements in both the  $(n,p)$  data and the  $(\mu^-, \nu)$  data. Note the  $\gamma$ -ray detection method in the muon capture experiment makes the  $^{23}\text{Na}$  g.s.  $\rightarrow ^{23}\text{Ne}$  g.s. transition unobservable.

states is  $0.74 \pm 0.09$  for the USD computation and  $1.11 \pm 0.13$  for the KUO computation, consistent with the different ‘‘best fit’’ values of  $\tilde{g}_a$  using the USD interaction ( $\tilde{g}_a = -1.01$ ) and the KUO interaction ( $\tilde{g}_a = -1.34$ ).

Finally, in Fig. 8 we compare the  $^{23}\text{Na}(n,p) 0^\circ$  cross section with the  $^{23}\text{Na}(\mu^-, \nu)$  capture distribution to the low-lying  $^{23}\text{Ne}$  levels. The resemblance reflects the importance of the GT matrix elements in the  $^{23}\text{Na} \rightarrow ^{23}\text{Ne}$  transitions observed via both the  $(n,p)$  and  $(\mu^-, \nu)$  reactions.

#### E. Extraction of $\tilde{g}_p/\tilde{g}_a$ from the $^{23}\text{Na} \rightarrow ^{23}\text{Ne}$ data

To extract the coupling constant ratio  $\tilde{g}_p/\tilde{g}_a$  we have fitted the calculated hyperfine dependences to the measured hyperfine dependences for the six observed  $^{23}\text{Na}(\mu^-, \nu)^{23}\text{Ne}^*$  transitions. The hyperfine dependences  $Y_S^{'+}/Y_S'^-$  listed in Table II include both direct and indirect capture to each state and were calculated via

$$\frac{Y_S^{'+}}{Y_S'^-} = \frac{\Lambda_S^{'+}}{\Lambda_S'^-} = \sum f_S^{S'} P_S^{S'} \frac{\Lambda_S^{'+}}{\Lambda_S'^-}, \quad (18)$$

where  $\Lambda_S^{'+}/\Lambda_S'^-$  is the hyperfine capture ratio for the state  $S'$  including only direct capture,  $\Lambda_S^{'+}/\Lambda_S'^-$  is the hyperfine capture ratio for the state  $S$  including both direct and indirect capture,  $P_S^{S'}$  is the parentage of the state  $S$  due to the state  $S'$ , and  $f_S^{S'}$  is a correction factor given by

$$f_S^{S'} = \frac{0.97 + 0.03 Y_{S'}^{'+}/Y_{S'}'^-}{0.97 + 0.03 \Lambda_S^{'+}/\Lambda_S'^-}. \quad (19)$$

In Eq. (18) the summation includes all states  $S'$  leading to the production of state  $S$  and the specific linear combination of direct capture ratios  $\Lambda_S^{'+}/\Lambda_S'^-$  in the direct and indirect capture ratios  $\Lambda_S^{'+}/\Lambda_S'^-$  ensures that the production of state  $S$  by capture to state  $S'$  is in accord with the measured par-

entages  $P_S^{S'}$ . The correction factors  $f_S^{S'}$ , which differ from unity by  $\leq 6\%$ , account for the observed capture rate being  $\Lambda_S^{\text{obs}} = 0.97\Lambda_S^- + 0.03\Lambda_S^+$ , not simply  $\Lambda_S^-$  (where  $f_S^{S'}$  would be unity).

To extract  $\tilde{g}_p/\tilde{g}_a$  from the hyperfine dependence data we have used Eqs. (12) and (13) for  $\Lambda^{\text{stat}}$  and  $\delta\Lambda^F$ , the formulas of Donnelly and Haxton for the  $\mathcal{L}_J$ ,  $\mathcal{M}_J$ ,  $\mathcal{T}_J^{\text{el}}$ , and  $\mathcal{T}_J^{\text{mag}}$  SPME's, and the OXBASH shell-model computer code for the OBTD's. In the fits we fixed the weak vector and magnetic couplings at  $g_v = 1.00$  and  $g_m = 3.706$  and the weak axial coupling at the values obtained from the corresponding KUO and USD calculation fits of the  $\mu^-$  capture rates. In both the KUO and USD computations varying the input value of  $\tilde{g}_a$  between 0.75 and 1.5 had little effect on the output value of  $\tilde{g}_p/\tilde{g}_a$ .

The values of  $\tilde{g}_p/\tilde{g}_a$  obtained from the fits were  $6.5 \pm 2.4$  for the USD interaction and  $7.9 \pm 2.2$  for the KUO interaction, where the quoted errors include experimental but not theoretical uncertainties. Comparisons of the measured and calculated hyperfine dependences using the ‘‘best fit’’ values of  $\tilde{g}_p/\tilde{g}_a$  and  $\tilde{g}_a$  are presented in Tables IV and V for the USD and KUO interactions, respectively. Both calculations show generally good agreement with the data although the USD calculation does better than the KUO calculation in the case of the weak 1702 and 2315 keV transitions.

The value of  $\tilde{g}_p/\tilde{g}_a$  obtained from the USD interaction fitted to the six hyperfine dependences is consistent with the two values of  $\tilde{g}_p/\tilde{g}_p$  of  $7.6 \pm_{2.5}^{2.1}$  and  $\leq 7.6$  extracted from the individual 1017 and 1823 keV hyperfine dependences in our earlier work [26]. The values of  $\tilde{g}_p/\tilde{g}_a$  obtained with the KUO and USD calculations are mutually consistent and agree with the predictions of PCAC and pion-pole dominance and the most recent analyses of the  $\mu^{-12}\text{C}$  and  $\mu^{-16}\text{O}$  OMC experiments. They do not indicate a large renormalization of  $\tilde{g}_p/\tilde{g}_a$  in  $^{23}\text{Na}$ . An important point is that the hyperfine dependence data determine  $\tilde{g}_p/\tilde{g}_a$  not  $\tilde{g}_p$ . Multiplying the values of  $\tilde{g}_p/\tilde{g}_a$  extracted from the hyperfine dependence data by the values of  $\tilde{g}_a$  extracted from the capture rate data to obtain  $\tilde{g}_p$  introduces additional uncertainties.

The Fujii-Primakoff approximation indicates that to the extent that GT matrix elements dominate other matrix elements, the value of  $\tilde{g}_p/\tilde{g}_a$  obtained from the hyperfine dependence data is nuclear model independent. Therefore it is important to ask, to what extent do the GT matrix elements dominate other nuclear matrix elements in the  $^{23}\text{Na} \rightarrow ^{23}\text{Ne}$  hyperfine dependence data, and to what extent does the value of  $\tilde{g}_p/\tilde{g}_a$  depend on the nuclear model? To answer these questions we used the results of Secs. VI C and VI D, which indicated (i) the GT matrix elements are rather well computed while the  $\ell = 2$  matrix elements are less well computed by the nuclear model, and (ii) the strong and intermediate 1017, 1823, 3432, and 3458 keV transitions are rather well predicted and weak 1702 and 2315 keV transitions less well predicted by the nuclear model.

In some  $^{23}\text{Na} \rightarrow ^{23}\text{Ne}$  transitions we found non-GT matrix elements play a small role in  $\Lambda_S^+/\Lambda_S^-$ . For example, in the case of direct  $F_+$  capture to the 1823 keV state, 83% of the rate is due to the GT matrix element alone, 12% of the rate is due to interference terms involving the product of GT and non-GT matrix elements, and 4% is due to non-GT ma-

trix elements alone. However, in other  $^{23}\text{Na} \rightarrow ^{23}\text{Ne}$  transitions non-GT matrix elements play a large role in  $\Lambda_S^+/\Lambda_S^-$ . For example, in the case of direct  $F_+$  capture to the 1017 keV state, 26% of the rate is due to the GT matrix element alone, 46% of the rate is due to interference terms involving the product of GT and non-GT matrix elements, and 27% is due to non-GT matrix elements. Consequently, cancellation of the nuclear model uncertainties in  $\Lambda_S^+/\Lambda_S^-$ , due to cancellation of the GT matrix elements in  $\Lambda_S^+/\Lambda_S^-$ , is not guaranteed. To gain insight into the relative role of the GT and non-GT matrix elements in the extraction of  $\tilde{g}_p/\tilde{g}_a$  from the hyperfine dependence data, we arbitrarily scaled all non-GT matrix elements relative to GT matrix elements by a factor of 1.50 in the fits. With the scaled non-GT matrix elements we obtained  $\tilde{g}_p/\tilde{g}_a = -6.6 \pm 2.3$  compared to  $\tilde{g}_p/\tilde{g}_a = -6.5 \pm 2.4$  with the USD interaction and  $\tilde{g}_p/\tilde{g}_a = -8.2 \pm 2.2$  compared to  $\tilde{g}_p/\tilde{g}_a = -7.9 \pm 2.2$  with the KUO interaction. For the USD interaction the ‘‘best fit’’ values of  $\Lambda_S^+/\Lambda_S^-$  for the 1017 keV transition changed from 0.14 to 0.17 and for the 1823 keV transition changed from 0.20 to 0.18 (the KUO interaction showed similar changes). These small differences in  $\tilde{g}_p/\tilde{g}_a$  and  $\Lambda_S^+/\Lambda_S^-$  suggest a mild overall dependence on the non-GT matrix elements.

The comparisons of the measured and calculated  $\mu^-$  capture rates suggested the weak 1702 and 2315 keV transitions were problematic. Therefore we repeated the fit of the hyperfine dependence data to  $\tilde{g}_p/\tilde{g}_a$  omitting either the 1702 keV transition or the 2315 keV transitions or both. In these fits  $\tilde{g}_p/\tilde{g}_a$  changed by no more than 0.4 for the USD calculation and 0.8 for the KUO calculation. The small changes in  $\tilde{g}_p/\tilde{g}_a$  reflect, in part, the small influence of the 1702 and 2315 keV transitions on the fit due to the large uncertainties in their values of  $Y_S^+/Y_S^-$ .

In conclusion, these tests suggest that the value of  $\tilde{g}_p/\tilde{g}_a$  extracted from the hyperfine dependence data is only mildly sensitive to the poorly known non-GT matrix elements and the poorly predicted 1702 and 2315 keV transitions.

### F. Undetected feeding of the $^{23}\text{Ne}$ states

A danger in the extraction of the effective couplings  $\tilde{g}_a$  and  $\tilde{g}_p/\tilde{g}_a$  is undetected feeding of the six observed  $^{23}\text{Ne}$  states. Undetected feeding, via  $\mu^-$  capture to higher energy  $^{23}\text{Ne}$  states, would increase the apparent capture rate and change the apparent hyperfine dependence, and thus cause errors in the extracted values of  $\tilde{g}_a$  and  $\tilde{g}_p/\tilde{g}_a$ .

Feeding of the observed  $^{23}\text{Ne}$  states from higher energy  $^{23}\text{Ne}$  bound states yields  $\gamma$  rays in the energy range 0–4 MeV (the neutron emission threshold is 5.193 MeV in  $^{23}\text{Ne}$ ). In both Ge1 and Ge2, excluding the  $\gamma$  rays from the 1017–3458 keV  $^{23}\text{Ne}$  states, we observed no other  $^{23}\text{Ne}$   $\gamma$  rays and no unidentified  $\gamma$  rays. We obtained, for known decays to the 1017–3458  $^{23}\text{Ne}$  states [49], the following approximate limits on feeding: 3836  $\rightarrow$  1017 was  $< 5\%$ , 3836  $\rightarrow$  1823 was  $< 5\%$ , 3988  $\rightarrow$  2315 was  $< 15\%$ , and 3836  $\rightarrow$  1702 was  $< 30\%$ . The poorer limits on feeding to the 1702 and 2315 keV states compared to the 1017 and 1823 keV reflects the lower yields of the former compared to the latter. These data established that undetected feeding due to any individual  $\gamma$  ray was small but not that undetected feeding due to several  $\gamma$  rays was small.

TABLE VIII. Calculated values of the polarization  $a_1$  and alignment  $a_2$  of the  $^{23}\text{Ne}$  recoil following muon capture on  $^{23}\text{Na}$  from the  $F_+$  and  $F_-$  hyperfine states. The values of  $a_1$  and  $a_2$  are calculated using the  $1s-0d$  shell model and the USD empirical effective interaction. They are calculated using (i) all nuclear matrix elements (denoted “all”) and (ii) only GT nuclear matrix elements (denoted “GT”).

$E_f$ (keV)	$J_f^\pi$	$a_1^+$ (all)	$a_2^+$ (all)	$a_1^-$ (all)	$a_2^-$ (all)	$a_1^+$ (GT)	$a_2^+$ (GT)	$a_1^-$ (GT)	$a_2^-$ (GT)
1017	$1/2^+$	0.279	0.000	-0.002	0.000	-0.200	0.000	-0.440	0.000
1702	$7/2^+$	0.707	-0.181	0.218	-0.981				
1823	$3/2^+$	-0.270	0.030	-0.039	-0.969	0.129	-0.178	0.574	-0.258
2315	$5/2^+$	0.952	0.098	0.546	-0.510	0.889	0.239	0.410	-0.748
3432	$3/2^+$	0.035	-0.189	0.169	-0.704	0.121	-0.176	0.550	-0.254
3458	$1/2^+$	-0.158	0.000	-0.031	0.000	-0.200	0.000	-0.437	0.000

To address the possibility of a number of individually insignificant  $\gamma$ -ray feedings leading to a collectively significant  $\gamma$ -ray feeding we measured the mean number of coincident  $\gamma$  rays for each of the nine observed  $^{23}\text{Ne}$   $\gamma$  rays. This quantity was determined by measuring the ratio of the  $\gamma$ -rays counts in the Ge1 singles and Ge1·CS2 coincidence spectra normalized to the ratio of the 1.33 MeV  $^{60}\text{Co}$   $\gamma$ -ray’s counts in the Ge1 singles and Ge1·CS2 coincidence spectra. We assumed no energy dependence for the CS2 photon acceptance and no directional correlation for the coincident  $\gamma$  rays (the method is primitive). We found the mean number of coincident  $\gamma$  rays for each of the observed  $^{23}\text{Ne}$   $\gamma$  rays was consistent with the  $\gamma$ -ray yield measurements of Table I. For the 1017 keV transition, the coincidence measurements gave  $0.56 \pm 0.03$  coincident  $\gamma$  rays per 1017 keV  $\gamma$  ray while the yield measurements predicted  $0.55 \pm 0.17$ , and for the 1823 keV transition, the coincidence measurements gave  $0.56 \pm 0.06$  coincident  $\gamma$  rays per 1823 keV  $\gamma$  ray while the yield measurements predicted  $0.63 \pm 0.16$ . Unfortunately, for the 1702 and 2315 keV transitions, where the measured yields are larger than the calculated yields, poor statistics prevented a useful comparison of the coincidence measurements and yield measurements. We cannot rule out feeding as the source of the difference in the calculated and measured yields for the 1702 and 2315 keV transitions.

Lastly, indirect evidence for the weakness of undetected feeding came from the  $^{23}\text{Na}(\mu^-, \nu)^{23}\text{Ne}$  shell model calculations and the  $^{23}\text{Na}(n, p)^{23}\text{Ne}$  experiment. Both the  $(\mu^-, \nu)$  calculations and the  $(n, p)$  experiment indicated 70–80% of the  $(\mu, \nu)$  or  $(n, p)$  strength to bound  $^{23}\text{Ne}$  states was to the six observed  $^{23}\text{Ne}$  states.

### G. Recoil orientation in muon capture on $^{23}\text{Na}$

Our tests of the relative role of GT and non-GT matrix elements in the extraction of  $\tilde{g}_p/\tilde{g}_a$  were somewhat crude. Here we suggest that measurements of the  $^{23}\text{Ne}$  orientation in the  $^{23}\text{Na}(\mu^-, \nu)^{23}\text{Ne}$  reaction would provide a more definitive test of the relative roles of the GT and non-GT terms and the model dependence of the extracted values of  $\tilde{g}_a$  and  $\tilde{g}_p/\tilde{g}_a$ .

Equations for the polarization  $a_1$  and alignment  $a_2$  of the recoil nucleus along the recoil direction have been published by several authors including Ciechanowicz and Oziewicz [53]. We have calculated  $a_1$  and  $a_2$  for the six  $^{23}\text{Na} \rightarrow ^{23}\text{Ne}$  transitions using Eq. (3.9) of Ref. [53], the formulas of

Donnelly and Haxton for the  $\mathcal{L}_J$ ,  $\mathcal{M}_J$ ,  $\mathcal{T}_J^{\text{el}}$ , and  $\mathcal{T}_J^{\text{mag}}$  SPME’s, and the  $1s-0d$  shell model with USD interaction for the OBTD’s. We used values of the weak coupling constants of  $g_v = 1$ ,  $g_m = 3.706$ ,  $\tilde{g}_a = -1.01$ , and  $\tilde{g}_p = 6.5$   $\tilde{g}_a$  (i.e., the “best fit” values of  $\tilde{g}_a$  and  $\tilde{g}_p/\tilde{g}_a$ ). The calculations were done using (i) all nuclear matrix elements, and (ii) only GT nuclear matrix elements.

Table VIII lists the resulting values of  $a_1$  and  $a_2$  for the six  $^{23}\text{Na} \rightarrow ^{23}\text{Ne}$  transitions. It indicates  $a_1$  and  $a_2$  can be very sensitive to non-GT matrix elements. For example, the alignment  $a_2$  in  $F_-$  capture to the 1823 keV  $^{23}\text{Ne}$  state is  $-0.97$  using all matrix elements and  $-0.26$  using only GT matrix elements, and the polarization  $a_1$  in  $F_-$  capture to the 1017 keV  $^{23}\text{Ne}$  state is 0.00 using all matrix elements and  $-0.44$  using only GT matrix elements. Measurements of either the recoil alignment or recoil polarization in  $^{23}\text{Na}(\mu^-, \nu)^{23}\text{Ne}^*$  would therefore be very valuable in examining the non-GT matrix elements and the nuclear model dependence of the values of  $\tilde{g}_a$  and  $\tilde{g}_p/\tilde{g}_a$  extracted from the capture rate and hyperfine dependence data.

## VII. SUMMARY

In summary, we have measured the capture rates and hyperfine dependences corresponding to 22  $\gamma$  rays and 17 states produced in muon capture on  $^{23}\text{Na}$  to various isotopes of Ne and F. The data include transitions to six low-lying states in  $^{23}\text{Ne}$ : two  $1/2^+$  states at 1017 and 3458 keV, two  $3/2^+$  states at 1823 and 3432 keV, one  $5/2^+$  state at 2315 keV and one  $7/2^+$  state at 1702 keV. Using the  $1s-0d$  shell model and the USD empirical effective interaction and KUO realistic effective interaction we have extracted “best fit” values of  $\tilde{g}_a$  and  $\tilde{g}_p/\tilde{g}_a$  from these data.

The resulting values of  $\tilde{g}_a$  obtained from fits to the capture rates are  $-1.01 \pm 0.07$  for the USD interaction and  $-1.34 \pm 0.08$  for the KUO interaction. The value of  $\tilde{g}_a$  extracted from the  $\mu^-$  capture data with the USD interaction is consistent with the values of  $\tilde{g}_a$  extracted from  $\beta^+/\beta^-$  decay and  $(p, n)/(n, p)$  charge exchange data also using the USD interaction. This builds confidence in the model’s application to  $\mu^-^{23}\text{Na}$ . The difference between the KUO and USD values of  $\tilde{g}_a$  was traced to systematically larger GT matrix elements in the KUO calculation than the USD calculation. The two calculations agreed with the measured  $\mu^-$  capture rates for the strong and intermediate 1017, 1823,

3432, and 3458 keV transitions but the calculated rates were smaller than the measured rates for the weak 1702 and 2315 keV states. This disparity was traced to the dominance of the GT matrix elements in the 1017, 1823, 3432, and 3458 keV capture rates but little or no contribution of the GT matrix elements in the 1702 and 2315 keV capture rates.

The ‘‘best fit’’ values of  $\tilde{g}_p/\tilde{g}_a$  obtained from fits to the hyperfine dependence data are  $6.5 \pm 2.4$  using the USD interaction and  $7.9 \pm 2.2$  using the KUO interaction. These values are in mutual agreement and are consistent with the predictions of PCAC and pion-pole dominance and earlier ordinary muon capture experiments on  $^{12}\text{C}$  yielding  $\tilde{g}_p/\tilde{g}_a = 8.5 \pm 1.9$  or  $9.7 \pm 1.7$  [13] and  $^{16}\text{O}$  yielding  $\tilde{g}_p/\tilde{g}_a$  7–9 [64]. Our results do not indicate a large renormalization of  $\tilde{g}_p/\tilde{g}_a$  in  $^{23}\text{Na}$  (a possible explanation of the nuclear RMC data). However, as discussed by Kirchbach and Riska [65], since OMC probes  $\tilde{g}_p$  at spacelike four-momentum transfer while RMC probes  $\tilde{g}_p$  at mainly timelike four-momentum transfer, a small renormalization of  $\tilde{g}_p$  in OMC but a large renormalization of  $\tilde{g}_p$  in RMC cannot be excluded. Comparison of the measured and calculated hyperfine dependences show generally good agreement between the models and the data, although the USD interaction did a better job than the KUO interaction for the weak 1702 and 2315 keV transi-

tions. Lastly, studies of the role of the rather well-known GT matrix elements and the less well known non-GT matrix elements in extracting  $\tilde{g}_p/\tilde{g}_a$  from the hyperfine dependence data suggest the results are only mildly nuclear model dependent.

Concerning future work, on the experimental side a determination of the recoil alignment or recoil polarization in muon capture on  $^{23}\text{Na}$  would be valuable in further testing the nuclear models used to extract  $\tilde{g}_a$  and  $\tilde{g}_p/\tilde{g}_a$  from the capture rate and hyperfine dependence data, while on the theoretical side an investigation of Wood-Saxon wave functions and Hartree-Fock wave functions rather than harmonic oscillator wave functions, and an examination of the assumption of a constant muon wave function over the nuclear volume, would be valuable.

We would like to thank Dr. Volodya Kuz'min and Dr. Tanya Tetereva for helpful discussions on theoretical issues and Dr. Jules Deutsch for helpful discussions on experimental issues. We would also like to thank the TRIUMF technical staff for the operation of the TRIUMF cyclotron and both the National Science Foundation (U.S.) and the Natural Sciences and Engineering Research Council (Canada) for their financial support.

- 
- [1] M. Gell-Mann and M. Levy, *Nuovo Cimento* **16**, 705 (1960).  
 [2] Y. Nambu, *Phys. Rev. Lett.* **4**, 380 (1960).  
 [3] M.L. Goldberger and S.B. Treiman, *Phys. Rev.* **110**, 1178 (1958).  
 [4] G. Bardin, J. Duclos, A. Magnon, J. Martino, A. Richter, E. Zavattini, A. Bertin, M. Piccinini, A. Vitale, and D. Measday, *Phys. Lett.* **104B**, 320 (1981), and references therein.  
 [5] M. Ericson, A. Figureau, and C. Thévenet, *Phys. Lett.* **45B**, 19 (1973).  
 [6] J. Delorme, M. Ericson, A. Figureau, and C. Thévenet, *Ann. Phys. (N.Y.)* **102**, 273 (1976).  
 [7] J. Delorme and M. Ericson, *Phys. Rev. C* **49**, 1763 (1994).  
 [8] M. Rho, *Annu. Rev. Nucl. Part. Sci.* **34**, 531 (1984).  
 [9] A. Possoz, D. Favart, L. Grenacs, J. Lehmann, P. Macq, D. Meda, L. Palfy, J. Julien, and C. Samour, *Phys. Lett.* **50B**, 438 (1974).  
 [10] L.Ph. Roesch, V.L. Telegdi, P. Truttman, A. Zehnder, L. Grenacs, and L. Palfy, *Phys. Rev. Lett.* **46**, 1507 (1981).  
 [11] Y. Kuno, J. Imazato, K. Nishiyama, K. Nagamine, T. Yamazaki, and T. Minamisono, *Phys. Lett.* **148B**, 270 (1984).  
 [12] Y. Kuno, J. Imazato, K. Nishiyama, K. Nagamine, T. Yamazaki, and T. Minamisono, *Z. Phys. A* **323**, 69 (1986).  
 [13] M. Fukui, K. Koshigiri, T. Sato, H. Ohtsubo, and M. Morita, *Prog. Theor. Phys. (Kyoto)* **78**, 343 (1987).  
 [14] M. Dobeli, M. Doser, L. van Elmbt, M.W. Schaad, P. Truol, A. Bay, J.P. Perroud, J. Imazato, and T. Ishikawa, *Phys. Rev. C* **37**, 1633 (1988).  
 [15] A. Frischknecht, M. Dobeli, W. Stehling, G. Strassner, P. Truol, J.C. Alder, C. Joseph, J.F. Loude, J.P. Perroud, D. Ruegger, M.T. Tran, and H. Panke, *Phys. Rev. C* **38**, 1996 (1988).  
 [16] D.S. Armstrong, S. Ahmad, R.A. Burnham, T.P. Goringe, M.D. Hasinoff, A.J. Larabee, C.E. Waltham, G. Azuelos, J.A. Macdonald, T. Numao, J.-M. Poutissou, M. Blecher, D.H. Wright, E.T.H. Clifford, J. Summhammer, P. Depommier, R. Poutissou, H. Mes, and B.C. Robertson, *Phys. Rev. C* **43**, 1425 (1991).  
 [17] D.S. Armstrong, A. Serna-Angel, S. Ahmad, G. Azuelos, W. Bertl, M. Blecher, C.Q. Chen, P. Depommier, T. von Egidy, T.P. Goringe, M.D. Hasinoff, R.S. Henderson, A.J. Larabee, J.A. Macdonald, S.C. McDonald, J.-M. Poutissou, R. Poutissou, B.C. Robertson, D.G. Sample, G.N. Taylor, D.H. Wright, and N.S. Zhang, *Phys. Rev. C* **46**, 1094 (1992).  
 [18] P. Christillin, *Nucl. Phys.* **A362**, 391 (1981).  
 [19] P. Christillin and M. Gmitro, *Phys. Lett.* **150B**, 50 (1985).  
 [20] P. Christillin, M. Rosa-Clot, and S. Servadio, *Nucl. Phys.* **A345**, 331 (1980).  
 [21] H.W. Fearing and M.S. Welsh, *Phys. Rev. C* **46**, 2077 (1992).  
 [22] M. Gmitro, A.A. Ovchinnikova, and T.V. Tetereva, *Nucl. Phys.* **A453**, 685 (1986).  
 [23] M. Gmitro, S.S. Kamalov, and A.A. Ovchinnikova, *Nucl. Phys.* **A468**, 404 (1987).  
 [24] M. Gmitro, S.S. Kamalov, F. Simkovic, and A.A. Ovchinnikova, *Nucl. Phys.* **A507**, 707 (1990).  
 [25] F. Roig and J. Navarro, *Phys. Lett. B* **236**, 393 (1990).  
 [26] T.P. Goringe, B.L. Johnson, D.S. Armstrong, J. Bauer, M.A. Kovash, M.D. Hasinoff, D.F. Measday, B.A. Mofteh, R. Porter, and D.H. Wright, *Phys. Rev. Lett.* **72**, 3472 (1994).  
 [27] N. Mukhopadhyay, *Phys. Rep.* **30C**, 1 (1977).  
 [28] A. Fujii and H. Primakoff, *Nuovo Cimento* **12**, 327 (1959).  
 [29] J.D. Walecka, *Nucl. Phys.* **A258**, 397 (1976).  
 [30] J. Bernébeu, *Nuovo Cimento* **4A**, 715 (1971).  
 [31] K. Koshigiri, H. Ohtsubo, and M. Morita, *Prog. Theor. Phys. (Kyoto)* **68**, 687 (1982).

- [32] K. Koshigiri, H. Ohtsubo, and M. Morita, *Prog. Theor. Phys.* (Kyoto) **71**, 1293 (1984).
- [33] V.A. Kuz'min, A.A. Ovchinnikova, and T.V. Tetereva, *Phys. At. Nuclei* **57**, 1881 (1994).
- [34] J.G. Congleton, *Phys. Rev. A* **48**, 12 (1993).
- [35] J.P. Deutsch, L. Grenacs, J. Lehmann, P. Lipnik, and P.C. Macq, *Phys. Lett.* **28B**, 178 (1968).
- [36] D. Favart, F. Brouillard, L. Grenacs, P. Igo-Kemenes, P. Lipnik, and P.C. Macq, *Phys. Rev. Lett.* **25**, 1348 (1970).
- [37] K. Ishida, J.H. Brewer, T. Matsuzaki, Y. Kuno, J. Imazato, and K. Nagamine, *Phys. Lett.* **167B**, 31 (1986).
- [38] R. Winston and V. Telegdi, *Phys. Rev. Lett.* **7**, 104 (1961).
- [39] R. Winston, *Phys. Rev.* **129**, 2766 (1963).
- [40] J.H. Brewer, *Hyperfine Interact.* **17–19**, 873 (1984).
- [41] T.P. Gorringer, B.L. Johnson, J. Bauer, M.A. Kovash, R. Porter, P. Gumplinger, M.D. Hasinoff, D.F. Measday, B.A. Mof-tah, D.S. Armstrong, and D.H. Wright, *Phys. Lett. B* **309**, 241 (1993).
- [42] L. Grenacs, J.P. Deutsch, P. Lipnik, and P.C. Macq, *Nucl. Instrum. Methods* **58**, 164 (1968).
- [43] T. Pratt, *Nucl. Instrum. Methods*, **66**, 348 (1968).
- [44] G.H. Miller, Ph.D. Dissertation, College of William and Mary, 1972 (unpublished).
- [45] F.J. Hartmann, T. von Egidy, R. Bergmann, M. Kleber, H.-J. Pfeiffer, K. Springer, and H. Daniel, *Phys. Rev. Lett.* **37**, 331 (1976).
- [46] P. Vogel, *Phys. Rev. A* **22**, 1600 (1980).
- [47] F.J. Hartmann, R. Bergmann, H. Daniel, H.-J. Pfeiffer, T. von Egidy, and W. Wilhelm, *Z. Phys. A* **305**, 189 (1982).
- [48] E. Storm and H.I. Israel, *Nuclear Data Tables* **A7**, 565 (1970).
- [49] P.M. Endt, *Nucl. Phys.* **A521**, 1 (1990), and references therein.
- [50] J. Bernstein, T.D. Lee, C.N. Yang, and H. Primakoff, *Phys. Rev.* **111**, 313 (1958).
- [51] T. Suzuki, D.F. Measday, and J.P. Roalsvig, *Phys. Rev. C* **35**, 2212 (1987).
- [52] J.D. Walecka, in *Muon Physics*, edited by C.S. Wu and V. Hughes (Academic, New York, 1975); J.D. Walecka, *Theoretical Nuclear and Subnuclear Physics* (Oxford University Press, New York, 1995).
- [53] S. Ciechanowicz and Z. Oziewicz, *Fortschr. Phys.* **32**, 61 (1984).
- [54] T.W. Donnelly and W.C. Haxton, *At. Data Nucl. Data Tables* **23**, 103 (1976).
- [55] B.A. Brown, A. Etchegoyen, W.D.M. Rae, and N.S. Godwin, The Oxford-Buenos-Aires-MSU shell-model code (OXBASH), MSUCL Report No. 524, 1986.
- [56] B.H. Wildenthal, in *Progress in Particle and Nuclear Physics*, edited by D.H. Wilkinson (Pergamon Press, Oxford, 1984), Vol. 11; B.A. Brown and B.H. Wildenthal, *At. Data Nucl. Data Tables* **33**, 347 (1985).
- [57] G.E. Brown and T.T.S. Kuo, *Nucl. Phys.* **85**, 40 (1966); T.T.S. Kuo, *Nucl. Phys.* **A103**, 71 (1967).
- [58] T. Hamada and I.D. Johnson, *Nucl. Phys.* **34**, 382 (1962).
- [59] B.J. Cole, A. Watt, and R.R. Whitehead, *J. Phys. G* **1**, 303 (1975).
- [60] B.A. Brown and B.H. Wildenthal, *Phys. Rev. C* **28**, 2397 (1983).
- [61] M.F. Jiang, R. Machleidt, D.B. Stout, and T.T.S. Kuo, *Phys. Rev. C* **46**, 910 (1991).
- [62] E.K. Warburton, *Phys. Rev. C* **45**, 463 (1992).
- [63] B. Siebels, T.P. Gorringer, J. Bauer, J. Evans, S. El-Kateb, K.P. Jackson, A. Trudel, and S. Yen, *Phys. Rev. C* **52**, 1488 (1995).
- [64] W.C. Haxton and Calvin Johnson, *Phys. Rev. Lett.* **65**, 1325 (1990).
- [65] M. Kirchbach and D.O. Riska, *Nucl. Phys.* **A578**, 511 (1994).